공학박사학위논문

은-금 코어-쉘 나노와이어의 3차원적 조립을 통한 고다공성·고전도성·생체친화성 템플릿 전극

Three-Dimensionally Assembled Ag-Au Core-Shell Nanowires as Highly Porous, Highly Conductive, and Biocompatible Template Electrodes

2023년 8월

서울대학교 대학원

기계공학부

최준화

은-금 코어-쉘 나노와이어의 3차원적 조립을 통한 고다공성 · 고전도성 · 생체친화성 템플릿 전극

Three-Dimensionally Assembled Ag-Au Core-Shell Nanowires as Highly Porous, Highly Conductive, and Biocompatible Template Electrodes

지도교수 고 승 환

이 논문을 공학박사 학위논문으로 제출함

2023년 4월

서울대학교 대학원

기계공학부

최 준 화

최준화의 공학박사 학위논문을 인준함

2023년 6월

위 원 장	차 석 원	(인)
부위원장	고 승 환	(인)
위 원	전 누 리	(인)
위 원	홍 석 준	(인)
위 원	이 하 범	(인)

Abstract

The fundamental characteristics of template electrodes, customized for various applications such as batteries, fuel cells, and bioelectrodes, significantly impact their overall performance. As a building block for next-generation template electrodes, core-shell nanowires have garnered significant interest due to the synergistic advantages offered by their core and shell materials. However, challenges such as scalability and dimensional constraints often limit their practical applications. This study introduces a highly porous Ag-Au core-shell nanowire foam (AACNF) that can be easily fabricated using a one-pot process based on nano-welding synthesis methods. To the best of the author's knowledge, the AACNF is a completely novel type of metal-based electrode, with the lowest density among metal-based electrodes while demonstrating high electrical conductivity (99.33 - 753.04 S m^{-1}). The AACNF's excellent mass transport properties enable multi-scale hierarchical incorporation of functional materials, including polymeric precursors and living cells. Due to nano-welded junctions, AACNF-hydrogel composites accomplished high mechanical stability against stretching (~700%) and exhibited 10,000 times higher conductivity than hydrogel-nanowire composites without the junction. Large particles in the 1-10 μm scale, including fibroblast cells and exoelectrogenic microbes, are also successfully incorporated with AACNF. AACNF-based microbial fuel cells show high power density (~330.1 W m^{-3}) within the optimal density range. The AACNF's distinctive ability to form a hierarchical structure with substances on various scales showcases its potential for advanced energy devices and bio-hybrid electrodes in the future.

Keyword : Ag-Au core-shell nanowire, 3D percolation network, Porous Template Electrode, Bio-hybrid electrode.

Student Number : 2018-25366

Table of Contents

Chapter 1. Introduction ····· 1

1.1. Study background ····· 1

1.2. Purpose of research ····· 2

Chapter 2. Fabrication ····· 6

2.1. Overview ····· 6

2.2. Fabrication Parameters ····· 7

2.3. General characterization ····· 12

2.4. Method ····· 18

Chapter 3. Mass Transporation in AACNF ····· 22

3.1. Overview ····· 22

3.2. Viscous Flow ····· 23

3.3. Microparticle ····· 27

3.4. Method ····· 31

Chapter 4. Application ····· 35

4.1. Integration with Hydrogels ····· 35

4.2. Microbial Fuel Cell ····· 41

4.3. Method ····· 49

Chapter 5. Conclusion and Perspectives ····· 52

Bibliography ····· 54

Abstract in Korean ····· 57

List of Figures

Figure 1. Examples of template electrodes. **(a)** Carbon paper. **(b)** Carbon cloth. **(c)** Graphene-oxide foam. **(d)** Ni foam. **(e)** Ag nanowire. **(f)** Cu foil with machined pores. ····· 2

Figure 2. Visualization of Ag and Au distribution in AACNF using SEM and EDS elemental mapping. ····· 3

Figure 3. The schematic illustration of the AACNF as template electrode for nanometer to micrometer scale substances. ····· 4

Figure 4. Hierarchical structures of AACNF with the PAAm hydrogel (a), PEDOT:PSS hydrogel **(b)**, the fibroblast cell **(c)**, and the *Geobacter Anodireducens* **(d)**. ····· 5

Figure 5. The schematic illustration of the fabrication principle for AACNF.

····· 6

Figure 6. The schematic illustration of the different states of PVP on the AgNW surface with respect to the existence of ethanol. ····· 6

Figure 7. Photographic images comparing the morphology of AACNF fabricated with (i) or without (ii) ethanol. ····· 7

Figure 8. (**a**) The morphology of the fabricated AACNF with respect to the ethanol volume fraction. (**b**) The plot of fabricated AACNF volumes against the precursor solutions and density of each AACNF according to the ethanol volume faction.

····· 9

Figure 9. (a) The morphology of the fabricated AACNF with respect to the weight ratio of the Au against the Ag. (**b**) ICP-MS analysis of the released Ag ions from AACNF after treatment of 2 M H_2O_2 for 30 min. ····· 10

Figure 10. The morphology of the fabricated AACNF (**a**) and the plot of electrical conductivity and density of the AACNF **(b)** with respect to the weight percent of NWs. ····· 11

Figure 11. Comparing AACNF and previously reported studies on the relationship between electrical conductivity and density. ····· 12

Figure 12. (**a**) Fabrication process of the sample for measuring the electrical conductivity of the AACNF over time. (**b**) Photographic images measuring the electrical conductivity of AACNF over time. ····· 14

Figure 13. Normalized electrical conductivity of the AACNF with varying densities against the synthesis time. ····· 1 4

Figure 14. (**a**) Photographic images of printed letter, "Ag Au" (i), and the printed letters seen through the 1 mm thick AACNF with 0.2 wt% of NWs (ii) and 0.5 wt% of NWs (iii). (**b**) The texts on the monitor screen which were seen through the AACNF with 0.2 wt% of NWs (i) and 0.5 wt% of NWs. ····· 1 5

Figure 15. Transmittance spectra of the 1 mm thick AACNF with varying densities by UV-Vis spectroscopy. ····· 1 6

Figure 16. (a) a photographic image of the UTM setup for compressive stress-strain curve measurements. **(b)** Compressive stress-strain curve of the AACNF with varying densities in water.····· 1 7

Figure17. (a) Examples of substances on the nanometer to micrometer scale that is permeable into AACNF. **(b)** The super-porous structure demonstrated by AACNF allows for rapid mass transfer of nanometer-scale substances. **(c)** Micrometer-scale particles exhibit different distributions along the depth-direction based on the density of AACNF. ····· 2 2

Figure 18. (a) AACNF samples to test the effect of the NW density. **(b)** The compression-mold for AACNF with NW densities from 1.0 to 4.0 wt%····· 2 4

Figure 19. (a) Diagram of the experimental setup diagram to measure viscous permeability of porous materials via pressure difference and mass flux across the media. **(b)** Photograph of the viscous permeability test.····· 2 4

Figure 20. (a) Viscous permeability against volumetric flux across the AACNF with different weight percent of NWs from 0.25 to 2.0. **(b)** Viscous permeability plotted against the weight percent of NWs, showing a drastic increase along with the decrease of the NW content. ····· 2 5

Figure 21. (a) Diagram of the two-chamber diffusion cell to measure the mass diffusivity across the porous material. **(b)** Photograph of the mass diffusivity test.

····· 2 5

Figure 22. (a) The glucose concentration over time measured from the receptor chamber according to varying densities of AACNFs. **(b)** Mass diffusivity of AACNF against glucose with respect to the weight percent of the NWs. ····· 2 6

Figure 23. The schematic illustration of cell-embedding, incubation and observation process.····· 2 8

Figure 24. The microscopic image (bright-field/live/dead) of L929 cells settled on the 3D nanowire matrix of AACNF (0.25 wt% NWs) at 36 h the cell viability **(a)**. Fluorescent calcein-AM images showing morphological changes of L929 cells

stretched to the direction of Ag-Au core-shell nanowires **(b-c)**. ····· 28

Figure 25. Seven days of viability test conducted on L929 cells showing the biocompatibility of AACNF. ····· 29

Figure 26. Microscopic images (DAPI) of L929-embedded AACNFs of varying NW densities, showing cell distribution by depths from the top surface. The L929 cells seeded on top of the AACNF and cultured for 36 h. ····· 30

Figure 27. The cell population ratio by depth from the top of the AACNF with varying densities. ····· 30

Figure 28. The schematic comparison of the PAAm hydrogel-embedded AACNF fabrication process **(a)** and the PAAm hydrogel with AgNWs **(b)**. ····· 35

Figure 29. The fabrication process for PAAm hydrogel-embedded AACNF. · 36

Figure 30. Electrical conductivity of the AACNF, PAAm hydrogel-embedded AACNF, and the PAAm hydrogel with AgNWs against the weight percent of the NWs. ····· 36

Figure 31. Photographic images of PAAm hydrogel-embedded AACNF with different NW content before and after stretching. ····· 37

Figure 32. Cross-sectional SEM images of the stretched PAAm hydrogel-embedded AACNF with different densities. AACNF with 0.4wt% of NW under 0% **(a)** and 300% **(b)** tensile strain. **(c)** phase-separated PAAm hydrogel-embedded AACNF(1.0 wt% of NWs) with 300% tensile strain. **(d)** Cracking of the agglomerated NWs networks ····· 38

Figure 33. (a) A photographic image of the PEDOT:PSS hydrogel-embedded AACNF before the cut. **(b)** A photographic image of the PEDOT:PSS hydrogel-embedded AACNF after the cut with a laser blade. (c) The optical microscope cross-sectional image of the PEDOT:PSS hydrogel-embedded AACNF. ····· 38

Figure 34. (a) Fabrication process of the sample for measuring the electrical conductivity of the PAAm hydrogel-embedded AACNF before and after stretching. (**b)** Photographic images measuring electrical conductivity before and after stretching the PAAm hydrogel-embedded AACNF. ····· 40

Figure 35. (a) Relative resistance with respect to the strain applied to the PAAm hydrogel-embedded AACNF with varying NW content. **(b)** Cyclic loading and unloading test to the PAAm hydrogel-embedded AACNF. ····· 40

Figure 36. (a) The schematic illustration of the operating mechanism of a single-chamber MFC using AACNF as an anode electrode. **(b)** Photographic image of a single-chamber MFC using AACNF as an anode electrode. ····· 42

Figure 37. SEM images of the *geobacter anodireducens* culture inside the AACNF **(a-c)** and on the dense 2D network of NWs**(d)**. ····· 4 2
Figure 38. Polarization curve **(a)** and power density curve **(b)** of the MFC using AACNF as an anode with respect to the microbial culture time. ····· 4 3

Figure 39. The analytic method of analyzing the polarization curve of a microbial fuel cell (MFC). ····· 4 5

Figure 40. (a) Polarization curves of the MFC with varying densities of the AACNF. **(b)** Activation loss (i), ohmic resistance (ii), limit current density (iii), and maximum power density (iv) of the MFC with varying densities of the AACNF.

····· 4 7

Figure 41. MFC maximum power against time for 25 days of long-term operation. The red arrow indicates the basal broth supply to the *Geobacter anodireducens* culture. ····· 4 8

Chapter 1. Introduction

1.1. Study Background

Porous electrodes have garnered significant attention from both academia and industry due to their various advantages and diverse applications in electrochemical systems, such as catalysts, batteries, and fuel cells [1-4]. The high surface area to volume ratio of porous electrodes is one of their primary benefits, as it enhances electrochemical reactions by providing more active sites for electron transfer and ion transport [5-8]. Another benefit of porous electrodes is their ability to facilitate the mass transport of reactants and products within the electrode structure, leading to increased uniformity of the overall reaction [2, 8]. In particular, porous electrodes based on nanomaterials, such as carbon nanotubes (CNTs) [9-11], graphene [12-16], transition-metal carbide (MXene) [17, 18], metal nanowires (NWs) [19-24], and hybrid complex [25-31] have undergone extensive research due to their ultralight, highly porous, and highly conductive properties [32, 33].

The core-shell structured nanowire (NW) has the potential to be an excellent candidate as a building block for porous electrodes, thanks to its enhanced functionalities achieved by combining different materials with complementary properties. The core can provide structural stability, while the shell can offer unique properties, such as improved electrical conductivity, chemical stability, or catalytic activity. This synergistic combination of materials in the core-shell structure results in NWs with enhanced functionalities that are not achievable with single-component NWs[34-42]. Especially, silver-gold (Ag-Au) core-shell nanowires (NWs) have emerged as promising nanomaterials with significant advantages, including high electrical conductivity and aspect ratio of the core AgNWs, and high chemical

stability of the Au shells [36-42]. These Ag-Au core-shell NWs exhibit excellent biocompatibility, making them promising candidates for porous electrodes in bioelectronic applications. Additionally, their corrosion resistance properties make them suitable for use in energy devices, further highlighting their potential in diverse electrochemical applications.

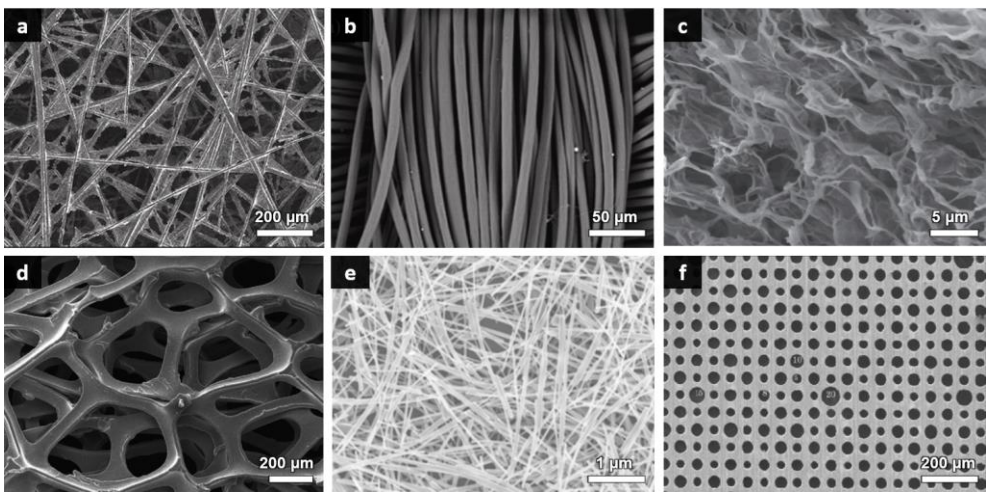

Figure 1. Examples of template electrodes with various size scale. **(a)** Carbon paper [60]. **(b)** Carbon cloth [61]. **(c)** Graphene-oxide foam [62]. **(d)** Ni foam [63]. **(e)** Ag nanowire [64]. **(f)** Cu foil with machined pores [65].

Despite the numerous advantages of the Ag-Au core-shell NW, their difficulties in the synthesis process have posed challenges in extending their applications to bulky three-dimensional (3D) porous electrodes over a millimeter-scale thickness. For various cases of porous materials, the pore size often correlates with the size scale of the backbones. As a result, when constructing porous electrodes with nanomaterials, they typically exhibit nanometer-scale pores and are commonly utilized as thin sheets or coated layers **(Figure 1)**. Most reported Ag-Au core-shell NWs based electrodes are limited to two-dimensional (2D) applications, such as

thin films or coatings [36-40]. To make 3D electrodes based on Ag-Au core-shell NWs, a common approach is to utilize them as a conductive filler within a polymer network [41, 42]. However, this approach requires excessive filler content to form a conductive path through the 3D NW percolation network, and these composites lack porosity because of the pre-existing polymer network. They have great features of both Ag-Au core-shell NWs and mechanical properties of the polymer, yet have difficulties in further coating process on the surface of NWs or making hierarchical structures with heterogeneous materials.

1.2. Purpose of Research

This paper introduces a straightforward method for synthesizing a 3D structure of Ag-Au core-shell nanowire foam (AACNF) with remarkable characteristics, including high porosity, electrical conductivity, and chemical stability. The presence of the Au shell of AACNF provides high chemical stability and biocompatibility, making it a suitable environment for living cells while the core AgNWs increase the aspect ratio and electrical conductivity to form a 3D percolation network with electrical paths (**Figure 2**).

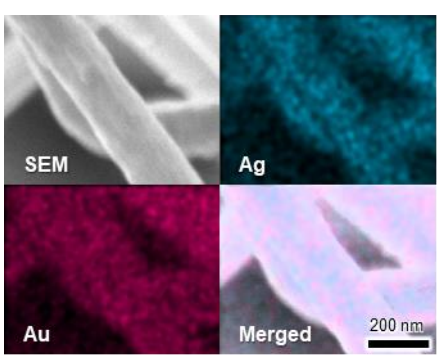

Figure 2. Visualization of Ag and Au distribution in AACNF using SEM and EDS elemental mapping.

Furthermore, the novel fabrication and optimizing process give the unique feature to the AACNF of a high porosity of over 99.9% and a large pore size of 1-10 μm, allowing for rapid mass transportation and the formation of a hierarchical structure with various scales of substances up to a few micrometers, including ions, hydrogel monomers, and living cells (**Figure 3**).

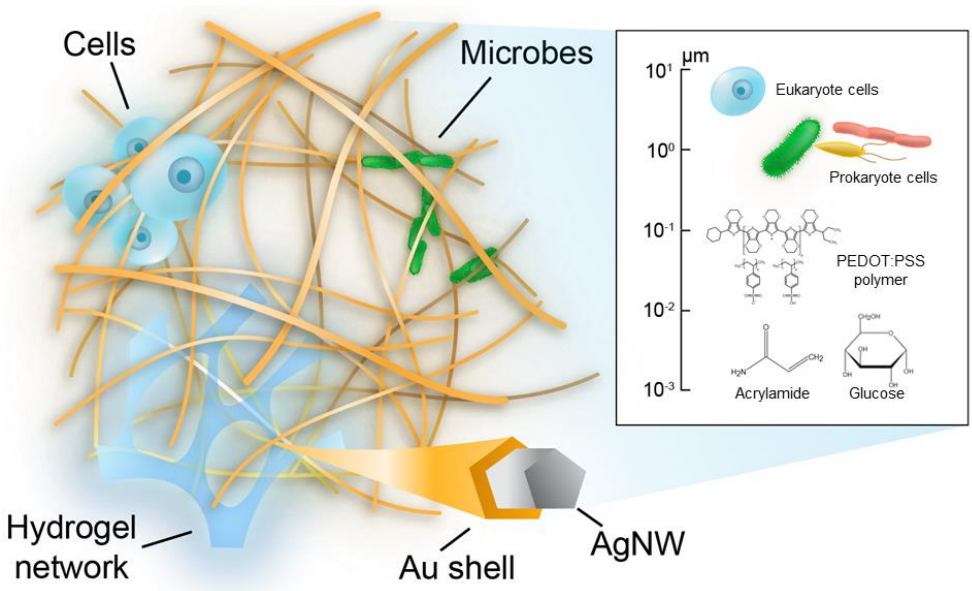

Figure 3. The schematic illustration of the AACNF as template electrode for nanometer to micrometer scale substances.

Utilizing the unique properties of AACNF, the author successfully fabricated composites of a hierarchical structure by integrating AACNF with other materials, including hydrogels such as polyacrylamide (PAAm) hydrogel or poly(3,4-ethylenedioxythiophene):poly(styrenesulfonate) (PEDOT:PSS) hydrogel, L929 cells (a fibroblast cell line derived from mice), and *Geobacter Anodireducens*, as

shown in **Figure 4**.

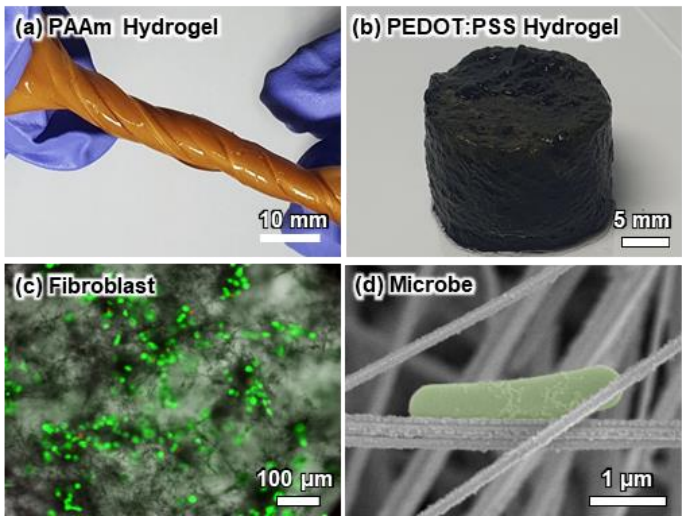

Figure 4. Hierarchical structures of AACNF with the PAAm hydrogel **(a),** PEDOT:PSS hydrogel **(b)**, the fibroblast cell **(c)**, and the *Geobacter Anodireducens* **(d)**.

This approach allowed us to create complex multi-component structures that could potentially be employed in diverse applications, such as energy storage, sensor, and biocompatible interfaces. The ability to fabricate 3D porous electrodes using AACNF opens up new avenues for the design of high-performance electrochemical devices that can operate at a larger scale.

Chapter 2. Fabrication

2.1. Overview

A simple one-step fabrication process was developed for synthesizing AACNF by mixing two solutions, the AgNW preparation solution and the Au precursor with ethanol (**Figure 5**).

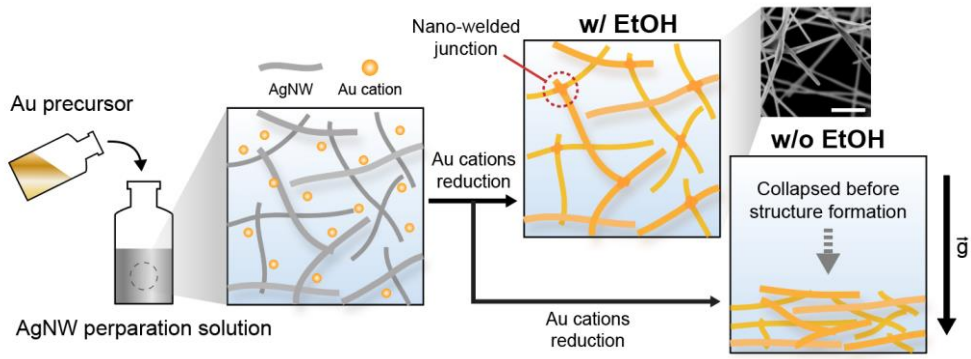

Figure 5. The schematic illustration of the fabrication principle for AACNF.

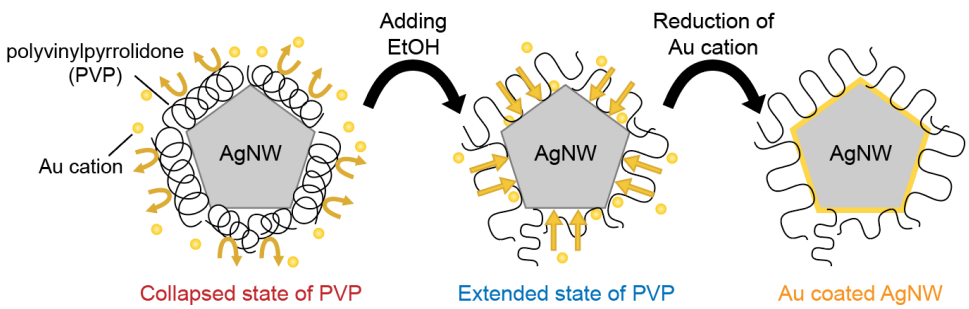

Figure 6. The schematic illustration of the different states of PVP on the AgNW surface with respect to the existence of ethanol.

Au cations are reduced by L-ascorbic acid (L-AA) on the surface of pristine AgNWs as the Au precursor is poured onto the AgNW preparation solution. In this

process, nano-welding occurs at the junction of the AgNW network simultaneously with the gold coating on the AgNW surface, forming a 3D percolation network. The Au shell of AACNF can enhance its chemical stability, making it suitable for forming hierarchical structures with living cells or maintaining its network integrity even in harsh environments. The 3D structure of AACNF is maintained by its nano-welded junctions, which enable the formation of robust electrical paths through a 3D percolation network of NWs.

To synthesize highly porous, mold-fitted, and chemically stable AACNF, three parameters—Ethanol concentration, Au against Ag ratio, and the precursor concentration—must be considered.

2.2. Fabrication Parameters

When a certain amount of Ethanol is mixed in the aqueous AACNF precursor solutions, it can lower the threshold density of the NW to form a 3D network and can form a mold-fitted structure of the AACNF (**Figure 7**).

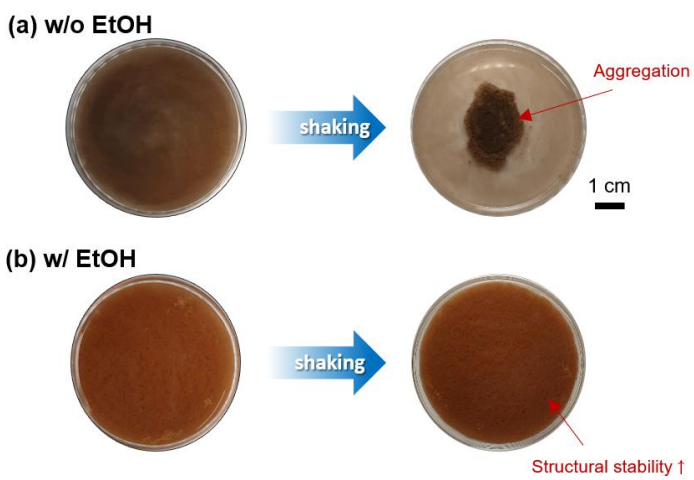

Figure 7. Photographic images comparing the morphology of AACNF fabricated without **(a)** or with **(b)** ethanol.

The effects of ethanol are assumed in two ways: the morphology changes of Polyvinylpyrrolidone (PVP) ligand in different solvents and the selective adsorption of ethanol to the PVP ligand of AgNW. Firstly, the morphology state of PVP varies depending on the solvent[43]. For PVP, water is a bad solvent, so PVP becomes a collapsed state. On the other hand, ethanol is a good solvent for PVP, and thus PVP becomes an extended state. Therefore, for higher ethanol fraction, Au cations could be more adsorbed to the AgNW surface as the PVP ligands of AgNW are more extended, which means that gold coating and nano-welding at the junction of AgNW are more facilitated (**Figure 6**). Secondly, PVP ligands of the AgNW preferentially adsorb ethanol more than water at an Ethanol molar fraction of less than 0.5 , thus Ethanol-dominant areas are formed on the AgNW surface. As the Ethanol-dominant areas merge, an ethanol-rich domain around the AgNW network is formed. When ethanol volume fraction against mixed solution is increased, the ethanol-rich domain becomes lighter and tends to rise to the water-air interface. As lightened AgNW network does not subside against gravity, a mold-fitted AACNF can be synthesized (**Figure 8a**, v/v = 0.2). However, when the ethanol volume fraction exceeds the optimum point, the ethanol-rich domain tends to rise too strongly, resulting in the formation of AACNF around the water-air interface (**Figure 8b**). Regarding this phenomenon, the author determined that 0.2 volume fraction of ethanol is suitable for AACNF preparation.

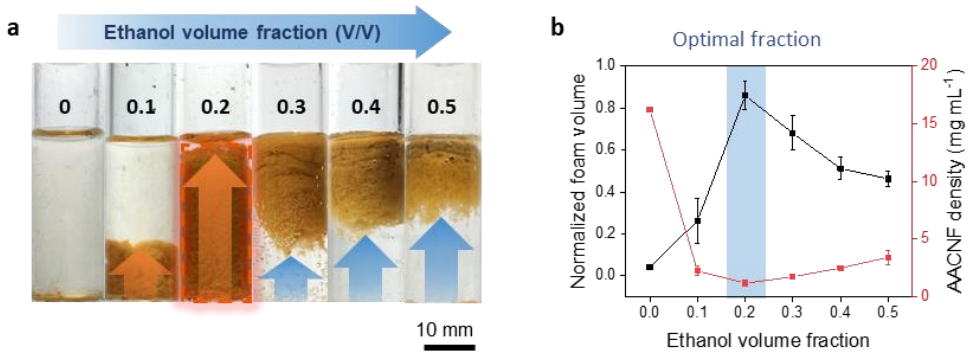

Figure 8. (a) The morphology of the fabricated AACNF with respect to the ethanol volume fraction. **(b)** The plot of fabricated AACNF volumes against the precursor solutions (left axis) and density of each AACNF (right axis) according to the ethanol volume faction. The weight ratio of the Au against the Ag was 3/4 and the weight percent of the NWs was 0.15. The error bars are the standard deviation (s.d.) for $N = 3$ samples.

The ratio of Au cations to the AgNWs is another important parameter to form mold-fitted, chemically stable AACNF. When the quantity of Au cations is insufficient, AACNF fails to maintain its structure and collapses to the floor of the mold due to the lack of nano-welded junctions. As the proportion of Au cations is increased, AACNF can be fitted to the mold while maintaining its shape with sufficient gold coating and nano-welded junctions (**Figure 9a**). Furthermore, the author conducted an inductively coupled plasma mass spectrometry (ICP-MS) analysis to quantify the degree of a gold coating of AACNF (after 30 min treatment of 2 M hydrogen peroxide (H_2O_2), (**Figure 9b**)). From these previous results, the author determined that the chemically stable and mold-fitted AACNF can be synthesized when the weight ratio of Au against Ag is 75% or higher.

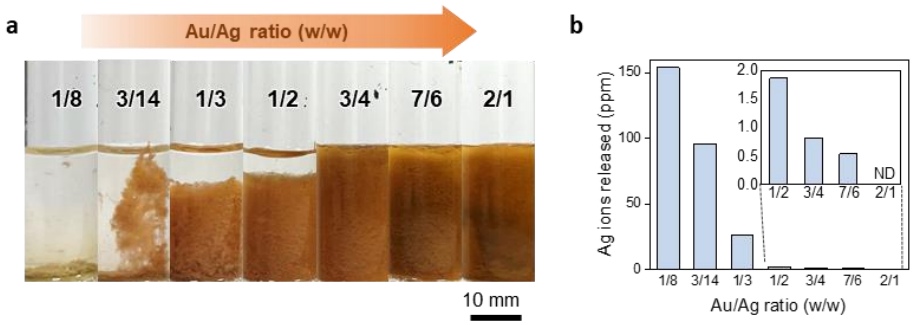

Figure 9. (a) The morphology of the fabricated AACNF with respect to the weight ratio of the Au against the Ag. **(b)** ICP-MS analysis of the released Ag ions from AACNF after treatment of 2 M H_2O_2 for 30 min. The ethanol volume fraction was 0.2 and the weight percent of the NWs was 0.25. ND, not detected.

After satisfying the two conditions mentioned earlier, the author synthesized AACNF by adjusting the concentration of reagents within the AgNW preparation solution and Au precursor. To quantitatively express the concentration of the reagents, we selected AgNWs as a representative parameter. The author modified the concentration of the AACNF reagents by adjusting the weight percent of the NWs while ensuring that the relative proportions of the other components remained consistent. This approach allowed us to control the concentration of the AACNF reagents in a precise manner while preserving the desired ratio between the components.

As the concentration of the AACNF reagents increases, a 3D percolation network of AgNW begins to form, and a bulk structure of AACNF is formed. In addition, increased junctions raise the stability of the network structure, thereby

improving the AACNF's resistivity against collapse. The mold-fitted AACNF formation threshold is 0.15 wt% of NWs where very porous and light foam is synthesized (**Figure 10a**). As the density of AACNF increased, electrical paths passing through the junctions of NWs increased; thus both density and electrical conductivity monotonically increased by 1.01 to 4.12 mg mL^{-1} and 99.33 to 753.04 S m^{-1}, respectively (**Figure 10b**).

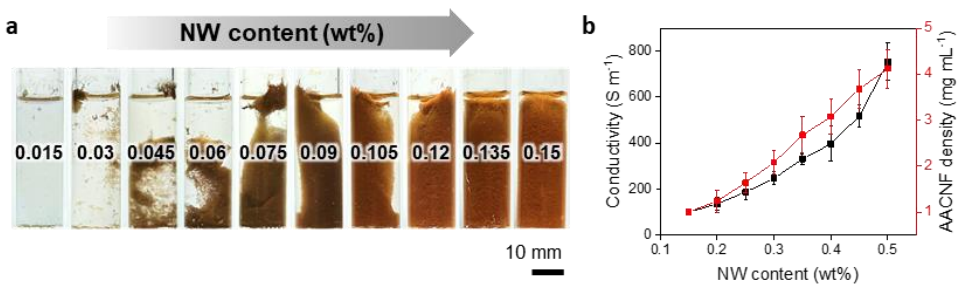

Figure 10. The morphology of the fabricated AACNF **(a)** and the plot of electrical conductivity (left axis) and density (right axis) of the AACNF **(b)** with respect to the weight percent of NWs. The ethanol volume fraction was 0.2 and the weight ratio of the Au against the Ag was 3/4. The error bars are the s.d. for $N = 3$ samples.

By using the optimized fabrication parameters, the author could synthesize the highly porous AACNF over 99.9% porosity. it has ultralow density (1.01 - 4.12 mg mL^{-1}) while demonstrating high electrical conductivity (99.33 - 753.04 S m^{-1}). To the best of the author's knowledge, this ultralight density region was first demonstrated compared to other NW-based porous electrodes (**Figure 11**).

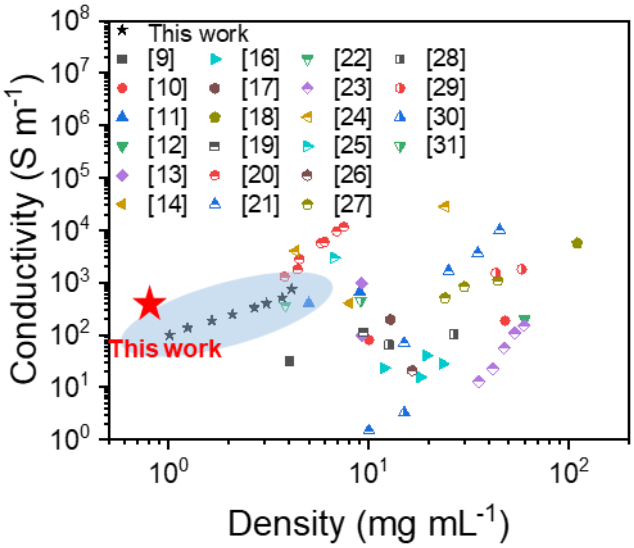

Figure 11. Comparing AACNF and previously reported studies on the relationship between electrical conductivity and density.

2.3. General Characterization

Proper acknowledgement of material properties is a crucial aspect of any research endeavor. In order to assess the material properties of AACNF, a series of characterization experiments were conducted. Given that AACNF does not conform to the typical profile of a conductive material, specific tests were implemented to effectively capture its distinctive attributes.

Electrical conductivity change of the AACNF over time

Two nickel foams (TNI0AH0001; TASCO) were placed at both ends of the Ecoflex (Ecoflex™ 00-30; Smooth-on) mold, and electrical resistance between them was measured and stored by connecting both nickel foams with a digital multimeter (DMM, DMM7510; Kiethly). When the AgNW preparation solution

and the Au precursor with ethanol were poured into the mold in order, AACNF was synthesized and electrically connected to both nickel foams. meanwhile, the DMM stored the electrical resistance between the nickel foams over time, which was the sum of the resistance of nickel foams and the resistance of AANCF. Thus, we calculated the resistance of the AACNF over time by subtracting the resistance of the nickel foams from the DMM measured data. Then, the electrical conductivities of the AACNF over time were calculated by the following equation: $\sigma = L/(R \cdot A)$. Photographic images of the measurement process are described in **Figure 12**.

Time-conductivity

To analyze the temporal tendency of AACNF synthesis after mixing the AgNW preparation solution and Au precursor with ethanol, we measured the normalized electrical conductivity of varying densities of AACNF with respect to synthesis time (**Figure 13**). Within 0.5 seconds after mixing, the electrical conductivity of AACNF with 0.2, 0.3, 0.4, and 0.5 wt% NWs immediately jumps to 12.770, 13.525, 21.155, and 19.582 times the initial conductivity, respectively. This immediate conductivity jump indicates the initial formation of AACNF and its electrical paths. After that, as nano-welding is strengthened by additional Au cations reduction, electrical conductivity gradually improves, and then saturated after about 2 h.

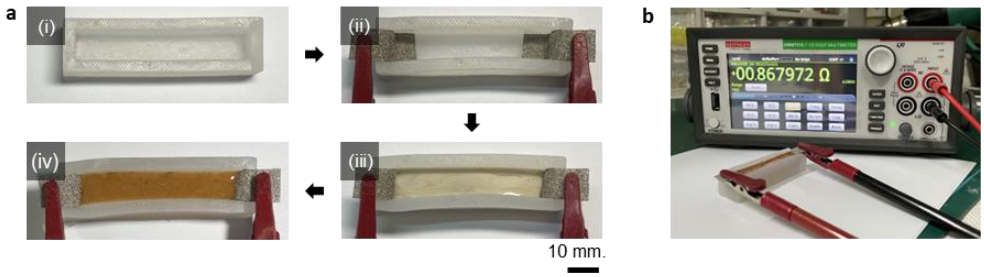

Figure 12. (a) Fabrication process of the sample for measuring the electrical conductivity of the AACNF over time. **(b)** Photographic images measuring the electrical conductivity of AACNF over time.

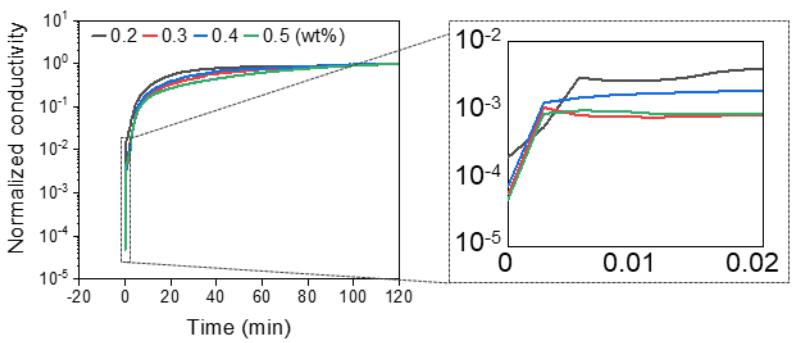

Figure 13. Normalized electrical conductivity of the AACNF with varying densities against the synthesis time.

Optical transmittance

To measure the transmittance spectra of AACNF, we did UV-Vis spectrophotometry analysis of 1 mm thickness AACNF for wavelength range from 330 nm to 800 nm (**Figure 15**). In this wavelength range, as density of AACNF increases, its porosity decreases and average transmittance decreases. Low density (0.2 wt% of NWs) AACNF has transmittance of about 30% in visible light range

(370 nm to 740 nm), with transparency to extent that printed letters or texts on monitor screen are visible through it, whereas high density (0.5 wt% of NWs) AACNF has transmittance of about 4% in visible light range which is not that transparent (**Figure 14**).

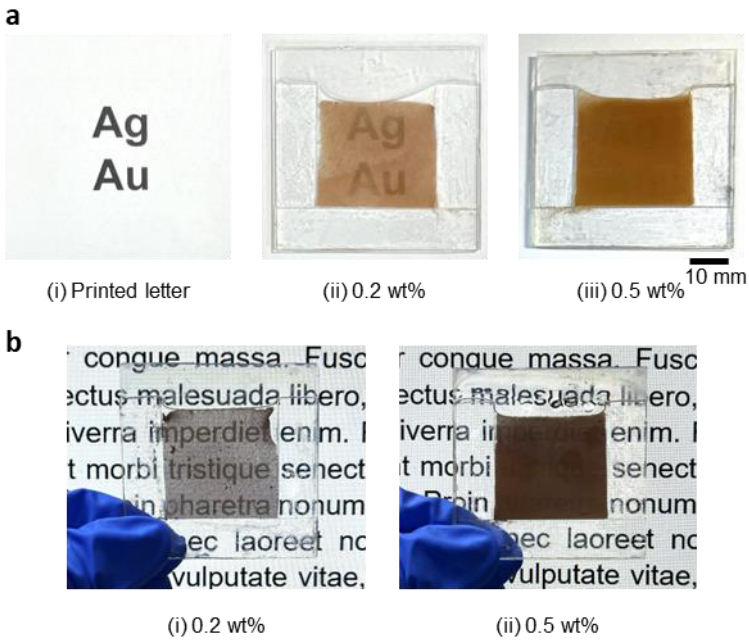

Figure 14. (a) Photographic images of printed letter, “Ag Au” (i), and the printed letters seen through the 1 mm thick AACNF with 0.2 wt% of NWs (ii) and 0.5 wt% of NWs (iii). **(b)** The texts on the monitor screen which were seen through the AACNF with 0.2 wt% of NWs (i) and 0.5 wt% of NWs.

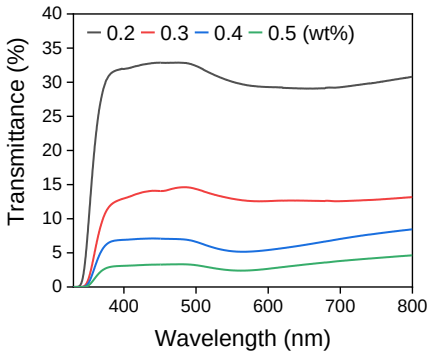

Figure 15. Transmittance spectra of the 1 mm thick AACNF with varying densities by UV-Vis spectroscopy.

Mechanical Properties

Due to the very low density of AACNF and thinness of NWs, AACNF couldn't withstand its structure out of water, as surface tension of water inside AACNF was removed. Thus, the author conducted compression test of AACNF inside water by universal test machine (UTM) to analyze mechanical behavior of AACNF inside water (**Figure 16a**). In order to remove influence of water pressure applied to UTM compression platens and interfacial tension between them, compressive force of plain water measured by UTM was subtracted from compressive force of AACNF in water measured by UTM (**Figure 16b**). It can be seen that as density of AACNF increased, mechanical robustness of AACNF increased. Additional freeze-drying or polymer network embedding would be considered as method for utilizing AACNF out of water.

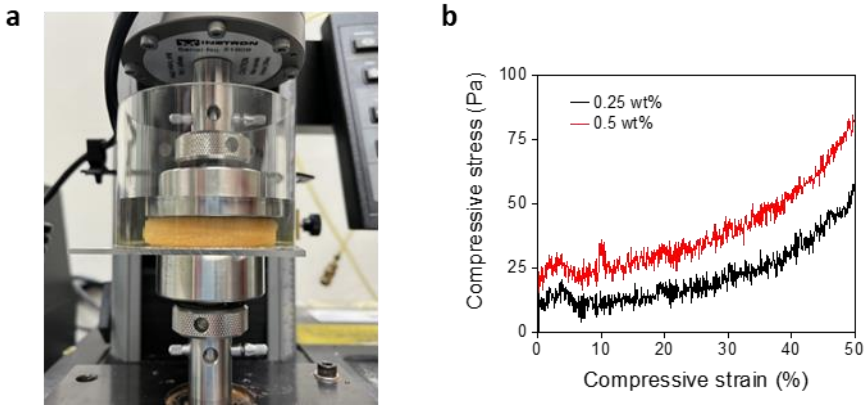

Figure 16. (a) a photographic image of the UTM setup for compressive stress-strain curve measurements. The diameter of the UTM compression platen was 50 mm, and the diameter and height of the AACNF were 41 mm and 20 mm. **(b)** Compressive stress-strain curve of the AACNF with varying densities in water. In order to remove the influence of the water pressure applied to the UTM compression platens and the interfacial tension between them, the compressive force of the water measured by UTM was subtracted from the compressive force of the AACNF in water measured by UTM.

2.4. Method

Materials

Polyvinylpyrrolidone (PVP, Mw = 360,000, Mw = 40,000), Copper(II) chloride dihydrate ($CuCl_2 \cdot 2H_2O$, 99.999%), Gold(III) chloride trihydrate ($HAuCl_4 \cdot 3H_2O$, ≥99.9% trace metals basis), Sodium sulfite (Na_2SO_3, ACS reagent, ≥98.0%), L-ascorbic acid (L-AA, ACS reagent, ≥99%), Acrylamide (AAm, suitable for electrophoresis, ≥99%), N,N′-methylenebis(acrylamide) (MBA, powder, for molecular biology, suitable for electrophoresis, ≥99.5%), D-(+)-Glucose (ACS reagent), and Ferric citrate (BioReagent, suitable for cell culture) were purchased from Sigma Aldrich.

Ethylene glycol (EG, 99.5%), Sodium hydroxide (NaOH, bead, 98%), Ammonium persulfate (APS, 98%), Sodium bicarbonate ($NaHCO_3$, 99.0-100.5%), Ammonium chloride (NH_4Cl, 99.0%), and Potassium chloride (KCl, 99.5%), and Sulfuric acid (95.0%) were purchased from Samchun Chemical Co., Ltd.

Silver(I) nitrate ($AgNO_3$, 99.9%) was purchased from Kojima Co., Ltd.

Sodium acetate (>98.5%) and Sodium dihydrogenphosphate, anhydrous (NaH_2PO_4, >99.0%) were purchased from KANTO CHEMICAL CO., INC.

Aqueous PEDOT:PSS dispersion (1.0 to 1.3 wt % solid content, Clevios™ PH 1000) was purchased from Heraeus Epurio LLC.

Synthesis of the AgNWs

AgNWs were synthesized by a polyol-mediated process, modified from a previous study . 3.182 g of PVP (Mw = 360,000) in 260 mL of EG was pre-heated at 175℃. After the temperature was saturated, 1.6 mL of 4 mM $CuCl_2 \cdot 2H_2O$ was added. After 10 mins, 60 mL of 98 mM $AgNO_3$ in EG is injected with the rate of 3 mL min-1. When the injection is finished, we stop the stirring and keep the synthesis reaction for 2 hours. As-synthesized AgNWs were diluted with acetone (5 times by volume) and the residual solution was removed to obtain aggregated NWs. Aggregated NWs were redispersed in distilled (DI) water and washed with centrifugation of 2500 rpm for 10 min several times. Finally, the purified AgNWs solution is adjusted to a concentration of 15.875 mg mL^{-1}.

Preparation of the AACNF

This recipe is for the AACNF with 0.25 wt% of NWs, 0.2 volume fraction of ethanol, and the 3/4 weight ratio of Au agaionst Ag. We synthesized Au precursor by mixing 0.095 M of $HAuCl_4 \cdot 3H_2O$ and 1 M of NaOH in a volume ratio of 1:1, and then mixing this mixture with 0.15 M of Na_2SO_3 in a volume ratio of 1:1. Then, we left Au precursor at room temperature undisturbed for 2 h. Additionally, We synthesized the AgNW preparation solution by orderly combining AgNWs (15.875 mg mL^{-1}), PVP (Mw 40,000; 7.2 wt%), 1.12 M of NaOH, 1.12 M of L-AA and 0.07 M of Na_2SO_3 by a volume ratio of 16:10:5:5:4. Finally, we mixed the Au precursor with ethanol in a volume ratio of 2:1, and then pour it into the AgNW preparation solution in a volume ratio of 2:3. This mixture was kept undisturbed at room temperature for 2 h to synthesize a sufficiently robust 3D structure of the AACNF.

Material Characterizations

SEM images were characterized by Field-Emission SEM (SUPRA 55VP; Carl Zeiss) and Energy Dispersive Spectroscopy (EDS) analysis was conducted to obtain the spatial distribution of elements of the samples. Transmittance of the AACNF of 1 mm thickness was analyzed by an ultraviolet-visible (UV-Vis) spectrophotometer (V-770; Jasco). A compression test of AACNF inside the water was conducted with a universal test machine (UTM, Instron-5543; Instron) with a speed of 0.005 s^{-1} to analyze the mechanical behavior of the AACNF inside the water. The electrical resistances of the AACNF and PAAm hydrogel-embedded AACNF were measured by the digital multimeter (DMM7510; Kiethly). The electrical conductivities of the samples were calculated by the following equation: $\sigma = L/(R \cdot A)$

Estimate the porosity of the AACNF

The porosity of the AACNF was estimated on the assumption that it consisted of only Ag and Au. The weight ratio of Au against Ag is 75%.

The density of the AACNF without the pore ρ_{AACNF} is calculated as below.

$$m_{\mathrm{Ag}} : m_{\mathrm{Au}} = 4 : 3 = \rho_{\mathrm{Ag}} V_{\mathrm{Ag}} : \rho_{\mathrm{Au}} V_{\mathrm{Au}} = 10.49\, V_{\mathrm{Ag}} : 19.3\, V_{\mathrm{Au}} \rightarrow V_{\mathrm{Ag}} = 2.4531\, V_{\mathrm{Au}}$$

$$(\rho_{\mathrm{Ag}} = 10.49\ \mathrm{g\ mL^{-1}}, \qquad \rho_{\mathrm{Au}} = 19.3\ \mathrm{g\ mL^{-1}})$$

$$\rho_{\mathrm{AACNF}} V_{\mathrm{AACNF}} = \rho_{\mathrm{AACNF}} \left(V_{\mathrm{Ag}} + V_{\mathrm{Au}}\right) = m_{\mathrm{AACNF}} = m_{\mathrm{Ag}} + m_{\mathrm{Au}}$$
$$= \rho_{\mathrm{Ag}} V_{\mathrm{Ag}} + \rho_{\mathrm{Au}} V_{\mathrm{Au}}$$

$$\rightarrow \rho_{\mathrm{AACNF}} = \frac{\rho_{\mathrm{Ag}} V_{\mathrm{Ag}} + \rho_{\mathrm{Au}} V_{\mathrm{Au}}}{V_{\mathrm{Ag}} + V_{\mathrm{Au}}} = \frac{(10.49 \times 2.4531) \times V_{\mathrm{Au}} + 19.3\, V_{\mathrm{Au}}}{3.4531\, V_{\mathrm{Au}}}$$
$$= 13.041 \text{ g mL}^{-1}$$

Then, the porosity of the AACNF ε is calculated as below.

$$\varepsilon = \frac{V_{\mathrm{V}}}{V_{\mathrm{T}}} = 1 - \frac{V_{\mathrm{AACNF}}}{V_{\mathrm{T}}} = 1 - \frac{\rho_{\mathrm{AACNF}}}{\rho_{\mathrm{T}}}$$

where V_{V} is the volume of the void space (pore), V_{T} is the total volume of the AACNF with pore, and ρ_{T} is the total density of the AACNF with pore.

As the density of the AACNF with pore is from 1.009 mg mL^{-1} to 4.117 mg mL^{-1}, the porosity of the AACNF could be calculated as 99.968 ~ 99.992 %.

Chemical stability test of the AACNF

To analyze the resistance of AACNF to oxidation, AACNF was treated with hydrogen peroxide (H_2O_2, 34.5% solution; Samchun Chemical Co., Ltd.), and the leakage amount of the Ag ions was measured. 3 mL of AACNFs with varying Au against Ag ratios were mixed with 27 mL of 2.22 M H_2O_2 solution to create an overall concentration of 2 M H_2O_2 with AACNF. The mixture was then incubated for 30 min at room temperature and the leaching solution was diluted with DI water and centrifuged for 2 min with 4000 RPM to remove the residual NWs. then, the transparent supernatant of the centrifuged solution is filtered through a 0.22 μm pore size filter to obtain a homogenous solution containing Ag ions. This final solution was analyzed by inductively coupled plasma mass spectrometry (ICP-MS, ELAN 6000; PERKIN-ELMER SCIEX) to quantify the amount of leaching Ag ions.

Chapter 3. Mass transportation in AACNF

3.1. Overview

The AACNF possesses an isotropic structure with uniquely high porosity, large pore size, and low tortuosity. These unique structural properties are anticipated to result in distinct mass transport characteristics. In this study, we examined the mass transfer properties of AACNF for substances ranging from nanometer-scale to micrometer-scale (**Figure 17a**). For nanometer-sized materials such as glucose, enzymes, and hydrogel monomers, their mass transport can be described either as bulk flow of the medium passing through AACNF or diffusion based on concentration gradient, as their size is considerably smaller than the pore size of AACNF (**Figure 17b**). Therefore, we investigated these two mechanisms of mass transportation passing through the AACNF with varying densities.

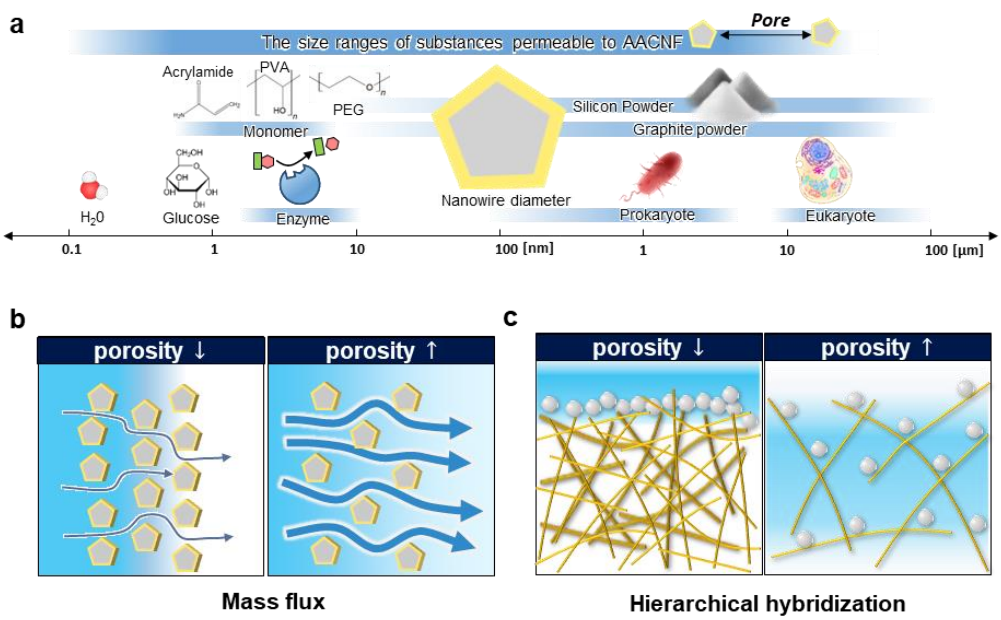

Figure 17. (a) Examples of substances on the nanometer to micrometer scale that is permeable into AACNF. **(b)** The super-porous structure demonstrated by AACNF

allows for rapid mass transfer of nanometer-scale substances. **(c)** Micrometer-scale particles exhibit different distributions along the depth-direction based on the density of AACNF. The super-porous structure first demonstrated in this study by AACNF enables the deep distribution of micrometer-scale particles.

3.2. Viscous Flow

Bulk flow of viscous fluids is inevitably affected by various geometrical characteristics inherent to porous materials. To investigate the effect of the density of AACNF over a wide range on the viscous permeability, we prepared high-density samples (1.0-4.0 wt% of NWs) by compressing samples with 0.5 wt% of NWs to 2-8 times their original thickness to the flow direction. The experimental setup depicted on **Figure 3b** was used to measure the viscous permeability of AACNF with varying densities **(Figure 18a-b,c)**. The result shows a significant difference in viscous permeability by the NWs content of AACNF, while exhibiting a slight increase with mass flux (**Figure 20a**). The re-plotted data of viscous permeability shows exponent increase along with the decrease of the AACNF density, which phenomenon accords with theoretical models on viscous permeability of porous material by random fiber structure [45]. The volumetric flux through AACNF rarely influences the overall curve form, indicating that the structure does not collapse under fluid flow(**Figure 20b**).

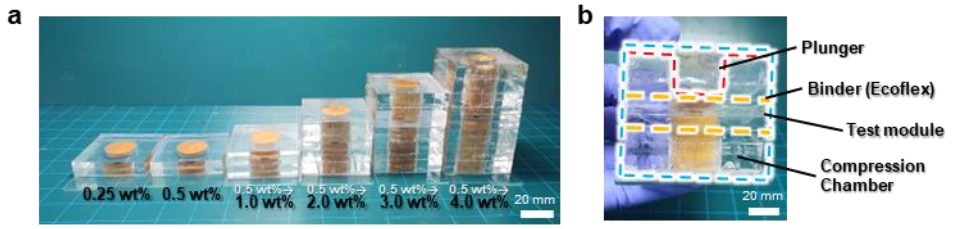

Figure 18. (a) AACNF samples to test the effect of the NW density. **(b)** The compression-mold for AACNF with NW densities from 1.0 to 4.0 wt%.

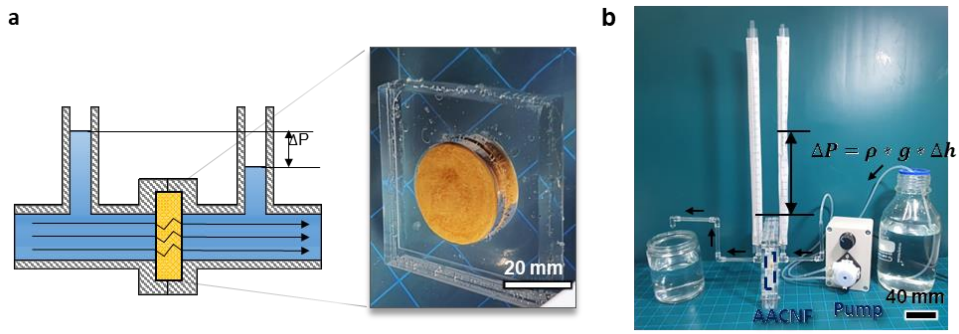

Figure 19. (a) Diagram of the experimental setup diagram to measure viscous permeability of porous materials via pressure difference and mass flux across the media. The image on the right shows the mounting configuration of an AACNF sample for the bulk flow and diffusion tests. **(b)** Photograph of the viscous permeability test. Each AACNF sample was inserted into the setup (blue square dotted-line), and hydraulic pressure was measured by observing the difference in water level on each side of the cylinders. (ΔP = (pressure difference of each side), ρ = (density of water), g = (acceleration of gravity), Δh = (difference of water level on each side)).

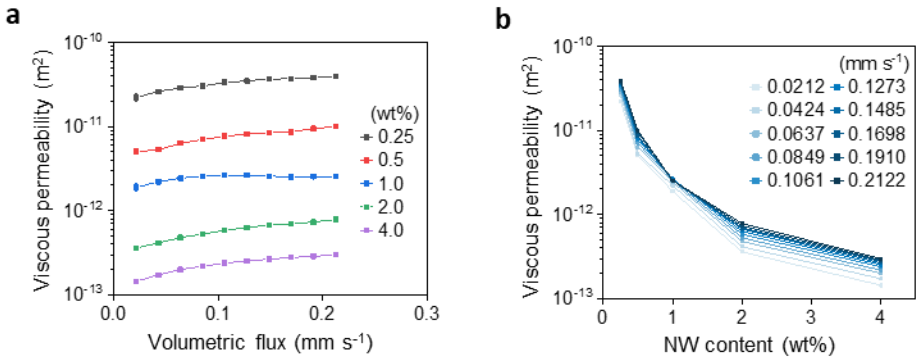

Figure 20. (a) Viscous permeability against volumetric flux across the AACNF with different weight percent of NWs from 0.25 to 2.0. The error bars are the s.d. for N = 5 samples. **(b)** Viscous permeability plotted against the weight percent of NWs, showing a drastic increase along with the decrease of the NW content. The error bars are the s.d. for N = 5 samples.

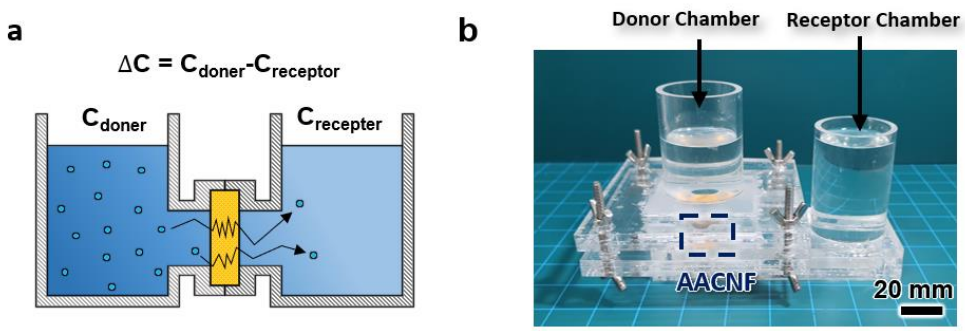

Figure 21. (a) Diagram of the two-chamber diffusion cell to measure the mass diffusivity across the porous material. **(b)** Photograph of the mass diffusivity test. Both chambers were filled with standard PBS solution. The donor chamber was supplied with glucose and the concentration of glucose diffused through the AACNF was measured at the receptor chamber.

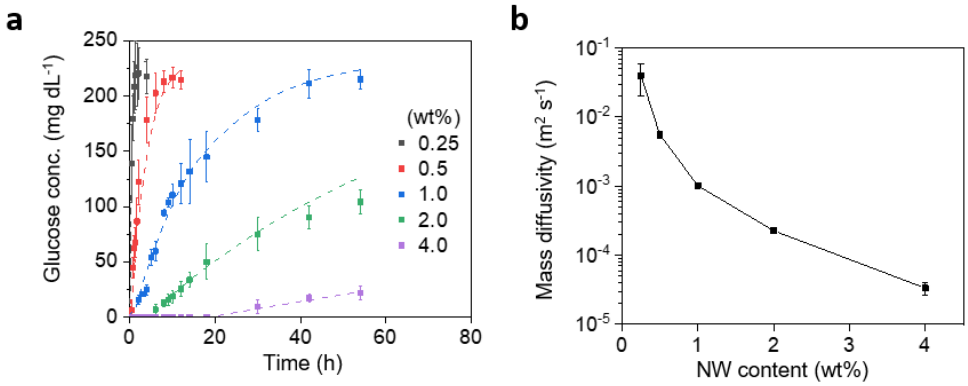

Figure 22. (a) The glucose concentration over time measured from the receptor chamber according to varying densities of AACNFs. The error bars are the s.d. for N = 8 samples. **(b)** Mass diffusivity of AACNF against glucose with respect to the weight percent of the NWs. The error bars are the s.d. for N = 8 samples.

Furthermore, we examined the diffusion phenomenon through AACNF under the condition where the dominant bulk fluid motion was absent, by tracking the change of glucose concentration by time using two-chamber diffusion cells (**Figure 21a-b**). The mass flux to the receptor chamber through the AACNF exhibited a definite difference with respect to the AACNF density (**Figure 3f**). The equivalent mass diffusivity, computed based on the profile of the glucose concentration over time, shows an exponential increase as AACNF density decreased. This trend is similar to that observed in the viscous permeability test (**Figure 3g**). The fitting equation for the mass diffusivity is available in the **Methods Section**.

3.3. Microparticle

In the context of AACNF, micrometer-scale materials can be regarded as large particles regarding the pore size. For the 1-10 μm scale range, there are various valuable components, including graphite and silicon particles frequently used in batteries, exoelectrogenic microbes utilized in biofuel cells, and eukaryotic cells that constitute the fundamental building blocks of living organisms . By tuning the porosity of AACNF via adjusting its density, AACNF can serve as a scaffold or a filter for these microparticles (**Figure 17c**). In this section, we aim to explore the potential for novel applications in energy devices or bio-hybrid electrodes enabled by this unique feature of AACNF, which has not been realized in other porous electrodes.

To investigate the interaction between microparticles and AACNF, as well as to explore the potential of AACNF for bio-interfacing electrode, we schemed to utilize the living cell as a tracer particle. We adopted L929 mouse fibroblast cells as they secrete extracellular matrix, hence have good adhesion with AACNF without any additional surface treatment. We seeded L929 cells onto the AACNF in culture media and observed the internal state of the L929-embedded AACNF by adjusting the focal plane of the microscopy, which was possible due to its transparency (**Figure 23**).

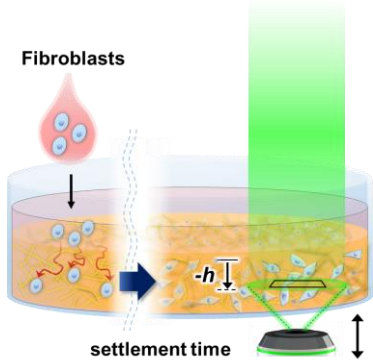

Figure 23. The schematic illustration of cell-embedding, incubation and observation process, with the L929 cells requiring 24-36 hours of settlement time. The transparency of AACNF allows for observation of the internal state of the matrix.

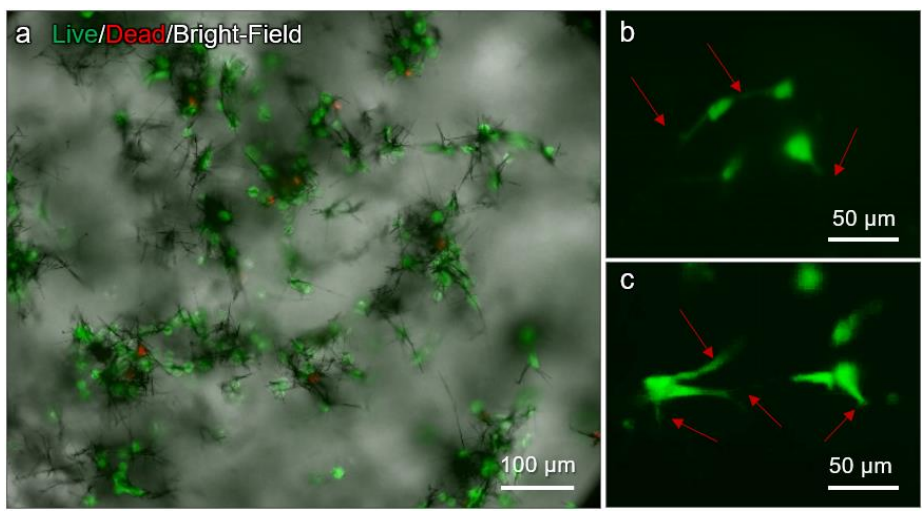

Figure 24. The microscopic image (bright-field/live/dead) of L929 cells settled on the 3D nanowire matrix of AACNF (0.25 wt% NWs) at 36 h the cell viability **(a).** Fluorescent calcein-AM images showing morphological changes of L929 cells stretched (arrow) to the direction of Ag-Au core-shell nanowires **(b-c).**

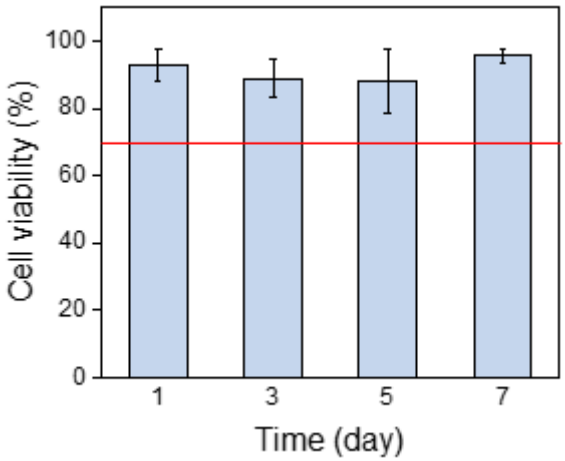

Figure 25. Seven days of viability test conducted on L929 cells showing the biocompatibility of AACNF.

After 36 hours of incubation, we used bright-field and fluorescent imaging to observe the viability **(Figure 24a)** and morphology change **(Figure 24b-c)** of L929 cells in AACNF. Due to AACNF's biocompatibility, L929 cells embedded in AACNF exhibit a high viability rate of over 88% throughout 7 days of incubation (**Figure 25**). The images obtained from different depths of L929-embedded AACNF reveal a clear difference in cell permeability depending on the density of AACNF. Specifically, while AACNF with a density higher than 0.5 wt% of NWs blocked the cell transfer into the matrix, AACNF with the lowest available density allowed for deep permeation into the matrix (**Figure 26**).

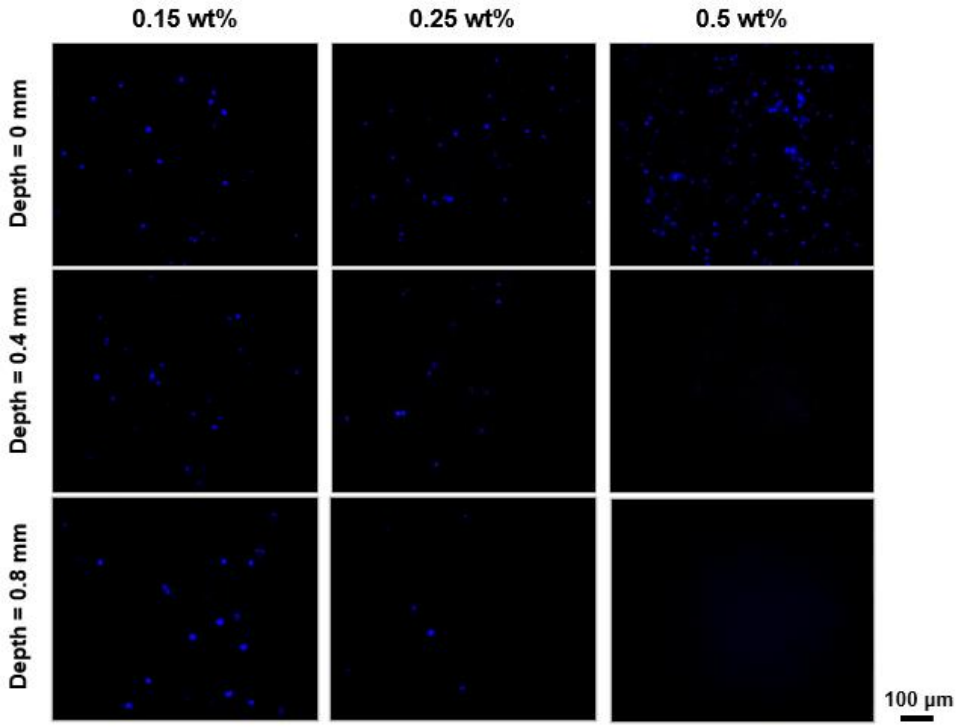

Figure 26. Microscopic images (DAPI) of L929-embedded AACNFs of varying NW densities, showing cell distribution by depths from the top surface. The L929 cells seeded on top of the AACNF and cultured for 36 h.

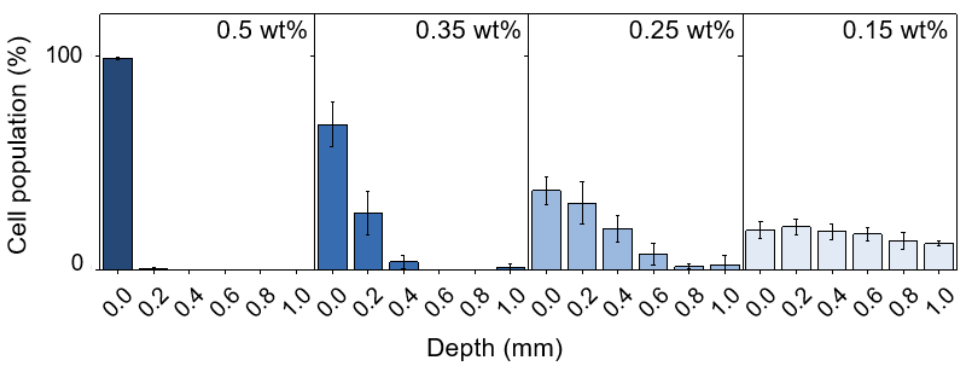

Figure 27. The cell population ratio by depth from the top of the AACNF with varying densities. The error bars are the s.d. for $N = 4$ samples.

To further estimate the spatial distribution of large particles in the AACNF, we evaluated the cell distribution along the perpendicular height for varying densities of AACNF with 0.15, 0.25, 0.35, and 0.5 wt% of NWs (**Figure 3j**). The representative samples of AACNF with varying densities are shown in **Figure S6c**. For sparse conditions of AACNF (0.15 wt% of NWs), L929 cells were distributed most evenly throughout the structure. For AACNF with 0.25 wt% and 0.35 wt% of NWs, L929 cells were observed throughout the complex but not as evenly distributed as in the 0.15 wt% of NWs. Under dense conditions of AACNF (0.5 wt% of NWs), transportation of L929 cells in the complex was blocked, and most cells accumulated on top of AACNF.

3.4. Method

Viscous permeability test

We measured the viscouse permeability, a viscous permeability of the water passing through the AACNF, by inserting AACNF like a filter into the manufactured chamber and passing a certain flux of water (0.0212, 0.0424, 0.0636, 0.0849, 0.1061, 0.1273, 0.1485, 0.1698, 0.1910, 0.2122 mm s^{-1}) by a motor pump. Then, the viscouse permeability could be calculated by substituting the pressure drop of water, obtained through the height of the water level rise, into the equation of Darcy's law below

$$q = -k\Delta P/(\mu L), \text{ where } \Delta P = \rho g \Delta h$$

where q is the flux of water passing through the AACNF, k is the viscouse permeability of the AACNF, μ is the dynamic viscosity of the water, L is the

thickness of the AACNF, ΔP is the pressure drop across the AACNF, ρ is the density of fluid, g is the gravitational acceleration, and Δh is the loss of the hydraulic head across the AACNF. By rearranging for k,

$$k = - q\mu L/\Delta P$$

Glucose diffusion test

We adopted typical diffusion experiment setup consisting of donor and receptor chambers and measured the changes of the glucose concentration of receptor chamber for each density of AACNF. Both solutions in two chambers filled with PBS and 580 mg dL^{-1} of glucose added into the 30 mL volume of donor chamber at t=0. The glucose concentration is sampled at the 45 mL volume of receptor chamber ofusing commercial glucose sensor (Glucolab; Osang Healthcare) with n = 8.

Mass diffusivity D_e is estimated using the fitting equation below.

By the law of conservation of mass,

$$C_d V_d + C_r V_r = \text{Const.} \qquad \Rightarrow \qquad \dot{C}_r = -\frac{V_d}{V_r}\dot{C}_d$$

For mass flux,

$$V_d \dot{C}_d = -\frac{D_e A}{l}(C_d - C_r)$$

Here, A, l, D_e refer to the area, thickness, and mass diffusivity of the AACNF, respectively. By combining the two equation above, we get

$$\ddot{C}_r + \alpha \dot{C}_r = 0, \qquad \text{where } \alpha = \frac{D_e A}{l}\left(\frac{1}{V_d} + \frac{1}{V_r}\right)$$

Then, the solution is as below.

$$C_r(\mathrm{t}) = \beta e^{-\alpha t} + \gamma$$

Applying boundary conditions: $C_r(0) = 0$ and

$$C_r(\infty) = C_d(\infty) = \frac{V_d}{V_d+V_r} C_d(0)$$

$$C_r(\mathrm{t}) = \frac{V_d}{V_d + V_r} C_d(0)(1 - e^{-\alpha t})$$

When rearranging for α in the equation above, we get the following:

$$\alpha = -\frac{\ln(1 - \frac{V_d + V_r}{V_d}\frac{C_r(\mathrm{t})}{C_d(0)})}{t}$$

We computed the value of α using least square method, and converted the result to the mass diffusivity D_e

Cell culture on AACNF

AACNFs were fabricated in a twelve-well plate (3513; Costar, MA, USA) with a 1 mm height, and with varying NW densities (0.15 wt%, 0.25 wt%, 0.35 wt%, and 0.5 wt%). After the synthesis of AACNF, the solution was exchanged three times with DI water and two times with Dulbecco's modified Eagle's medium (DMEM) (11885-084; Thermo Fisher Scientific, MA, USA) containing 10% fetal bovine serum serum (F2442; Sigma-Aldrich, MO, USA) and Anti-Anti (15240-062; Thermo Fisher Scientific), to ensure purity and appropriate nutrient conditions for cell culture. To ensure sufficient diffusion time, the replacing solution was added prior to each exchange process. The fully mixed solution was then removed after two hours for the DI water exchange steps, and after eight hours for the culture solution exchange steps.

Cell viability test

L929 mouse fibroblast cells (KCLB, Seoul, South Korea) were seeded at a density of 40,000 cells/cm^2 into a twelve-well plate with AACNF in culture media (n = 10). After incubation for 1, 3, 5 and 7 days at 37°C with 5% CO_2, a live and dead assay was performed using the LIVE/DEAD Viability/Cytotoxicity Kit (L3224; Invitrogen, CA, USA). In brief, 4 μM ethidium homodimer-1 and 2 μM calcein were added for 1 hour, and live (green) or dead (red) cells were observed and counted under a Nikon Eclipse Ti fluorescence microscope (Nikon Instruments Inc., NY, USA).

3D cell distribution analysis

L929 cells were dispersed on top of the AACNF in the culture solution with 40,000 cell cm^{-2}, and incubated the samples at 37ºC for 36 h. After 36 hours of incubation at at 37°C with 5% CO_2, bright-field images were obtained using the Nikon Eclipse TS100 microscope (Nikon, Japan) to analyze cell morphology changes. For locate the L929 cells effectively, the nuclei were stained using 4′,6-diamidino-2-phenylindole (D1306; Invitrogen), and the fluorecent images of the L929 embedded in AACNF were captured using a Nikon Eclipse Ti fluorescence microscope (Nikon Instruments Inc.) and NIS-Elements software (Nikon). To obtain internal images of the L929-embedded AACNFs, the microscope's focal plane was adjusted to capture images at various depths from the bottom (0 mm) to the top (1 mm) of the samples in increments of 0.2 mm. The distribution of L929 cells within the porous material was quantified based on the focal position of the cell nuclei.

Chapter 4. Applications

4.1. Hydrogel Integration

The highly porous nature of AACNF makes it a suitable candidate for containing heterogeneous materials and forming a hierarchical structure. In this study, we synthesized a hierarchical structure within AACNF by embedding PAAm hydrogel and PEDOT:PSS hydrogel. For PAAm hydrogel-embedded AACNF, we diffused hydrogel monomers (Acrylamide, AAm), crosslinkers (N,N′-methylenebis(acrylamide), MBA), and initiators (Ammonium persulfate, APS) inside the pore of the AACNF, followed by thermal polymerization (**Figure 28a)** and **Figure 29**) .

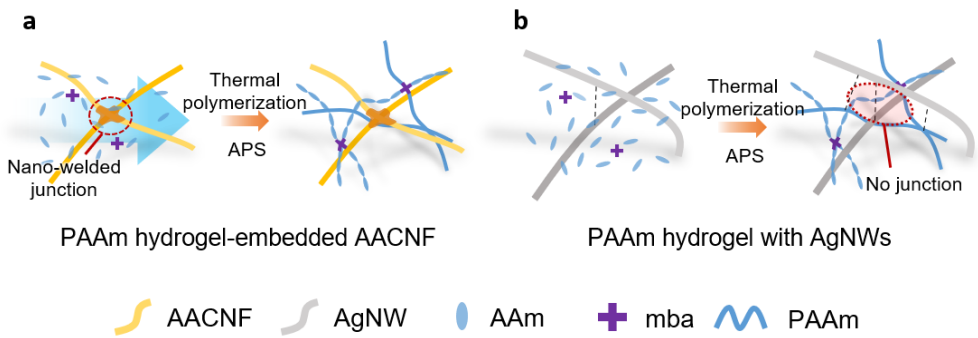

Figure 28. The schematic comparison of the PAAm hydrogel-embedded AACNF fabrication process **(a)** and the PAAm hydrogel with AgNWs **(b).**

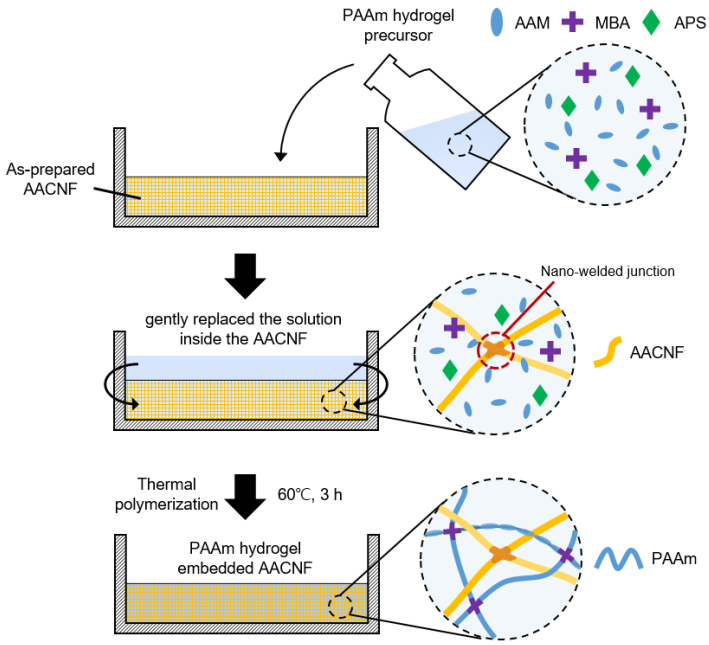

Figure 29. The fabrication process for PAAm hydrogel-embedded AACNF.

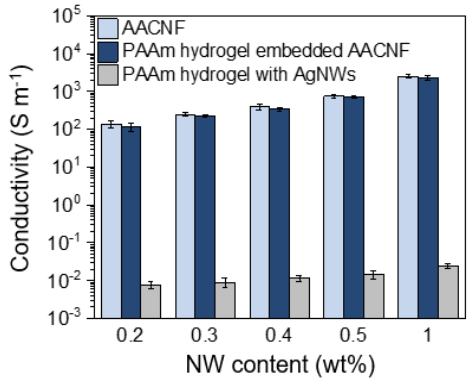

Figure 30. Electrical conductivity of the AACNF, PAAm hydrogel-embedded AACNF, and the PAAm hydrogel with AgNWs against the weight percent of the NWs. The error bars are the s.d. for $N = 3$ samples.

The PAAm hydrogel-embedded AACNF exhibited greate elasticity, which is an intrinsic property of the PAAm hydrogel. For PEDOT:PSS hydrogel-embedded AACNF, PEDOT:PSS polymer dispersion was permeated into the AACNF and treated with sulfuric acid . The resulting composites of AACNF with both hydrogels was confirmed by optical microscope and Scanning Electron Microscope (SEM) observations (**Figure 31 and 32c)**. The cut cross-section of the PEDOT:PSS hydrogel embedded AACNF shows the uniformly integrated PEDOT:PSS polymer network inside the AACNF **(Figure 33a-b)**.

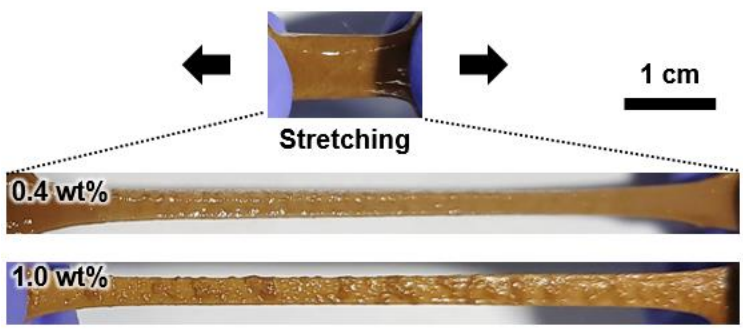

Figure 31. Photographic images of PAAm hydrogel-embedded AACNF with different NW content before and after stretching.

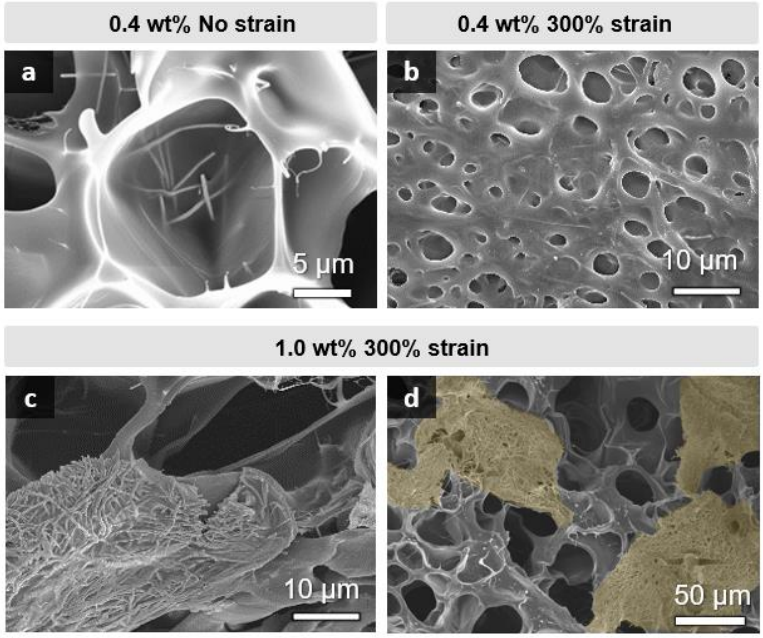

Figure 32. Cross-sectional SEM images of the stretched PAAm hydrogel-embedded AACNF with different densities. AACNF with 0.4wt% of NW under 0% **(a)** and 300% **(b)** tensile strain. **(c)** phase-separated PAAm hydrogel-embedded AACNF(1.0 wt% of NWs) with 300% tensile strain. **(d)** Cracking of the agglomerated NWs networks.

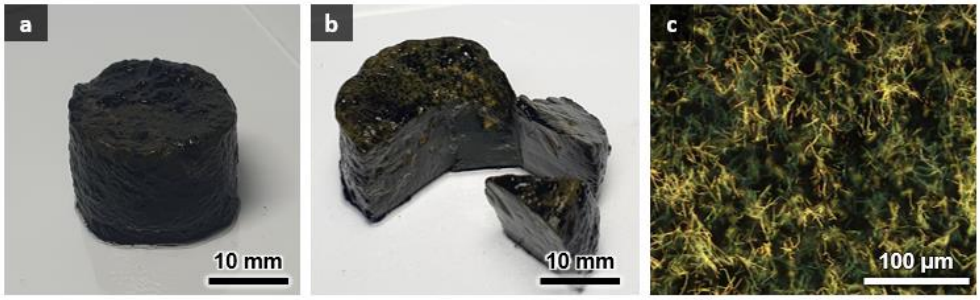

Figure 33. (a) A photographic image of the PEDOT:PSS hydrogel-embedded AACNF before the cut. **(b)** A photographic image of the PEDOT:PSS hydrogel-embedded AACNF after the cut with a laser blade. **(c)** The optical microscope cross-sectional image of the PEDOT:PSS hydrogel-embedded AACNF.

Due to the robustness of the electrical path provided by the nano-welded junctions between the NWs (**Figure 28a**), forming a PAAm hydrogel network inside the AACNF did not cause significant changes in electrical conductivity (**Figure 30**). It is worth noting that the electrical conductivity of the PAAm hydrogel-embedded AACNF with pre-formed nano-welded junctions is at least 10,000 times higher compared to a similar complex employing AgNWs as conducting fillers for PAAm hydrogel without such nano-welded junctions (**Figure 28b**).

The electrical conductivity of the PAAm hydrogel-embedded AACNF was also investigated under an external tensile strain of 0.1 s^{-1} speed. As the density of the AACNF increased to an optimal point (0.2 wt% to 0.4 wt% of the NWs), the electrical conductivity changes under external tensile strain decreased as the junctions of the NW network increased (**Figure 34a**). However, if the density of the AACNF exceeded the optimum point, the electrical conductivity retention of the composite under tensile strain was weakened (**Figure 34a**, 0.5 and 1.0 wt% of NWs). This was hypothesized to be due to an inability to uniformly disperse the hydrogel materials at densities of AACNF above the optimum point because of its relatively low permeability, resulting in a phase separation between the AACNF and hydrogel network, leading to cracks at conductive path under tensile stress (**Figure 31** and **32**). Additionally, it was found that electrical conductivity of composite was stable under repeated loading-unloading of 50% external strain over 1000 cycles (**Figure 34b**).

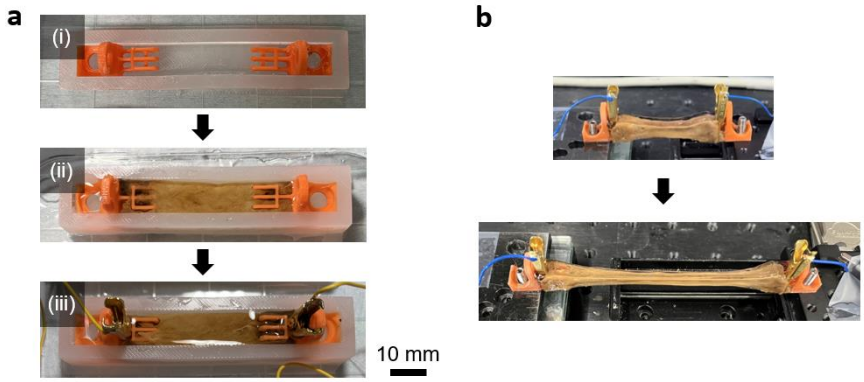

Figure 34. (a) Fabrication process of the sample for measuring the electrical conductivity of the PAAm hydrogel-embedded AACNF before and after stretching. **(b)** Photographic images measuring electrical conductivity before and after stretching the PAAm hydrogel-embedded AACNF.

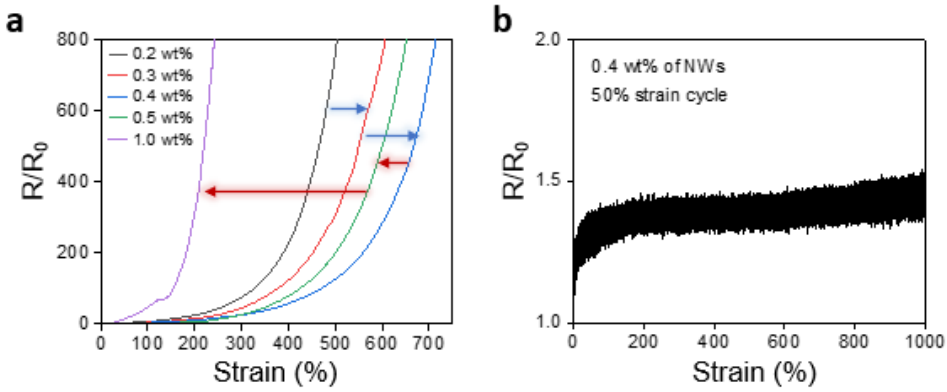

Figure 35. (a) Relative resistance with respect to the strain applied to the PAAm hydrogel-embedded AACNF with varying NW content. **(b)** Cyclic loading and unloading test (50% tensile strain, 12 s $cycle^{-1}$) to the PAAm hydrogel-embedded AACNF. The weight percent of NWs was 0.4.

4.2. Microbial Fuel Cell

The 3D cell culture has gained significant interest because planar cell structure inaccurately represents the 3D microenvironment [52]. The 3D cell structure is essential in biological advancement because it allows cells to cultivate and network with other cells and their environment much more efficiently than planar cell structure [53, 54]. Also, unlike 2D planar structure, 3D bulk interface of cell and electrode provides volumetric interface of the living cell and the electrode, and may utilized as an effective way of cell stimulation or harvesting energy. However, since the loss of cellular attachment usually leads to apoptosis, providing cells with a scaffold is crucial. AACNF contains great possibilities for 3D cell culture due to its inherent qualities such as ultrahigh porosity (>99.9%), tunable pores, excellent conductivity, bio-compatibility and non-corrosive nature. The ultrahigh porosity and tunable pores attribute of AACNF could provide an ideal 3D scaffold for various types of cells. Typically, Prokaryotic cells' size varies from 0.5μm to 5μm while in case of eukaryotic cells it varies from 10 μm to 100 μm.

In this study, we used AACNF as a 3D scaffold and culturing base for microbes to exploit the electrochemical activity of living cells. We used *Geobacter Anodireducens*, one of the exoelectrogenic bacteria, as the biocatalyst to develop a microbial fuel cell (MFC). The Geobacter-AACNF bio-hybrid composite was utilized as the anode, emitting electrons with hydrogen ions through biochemical reaction (**Figure 36a-b, c**).

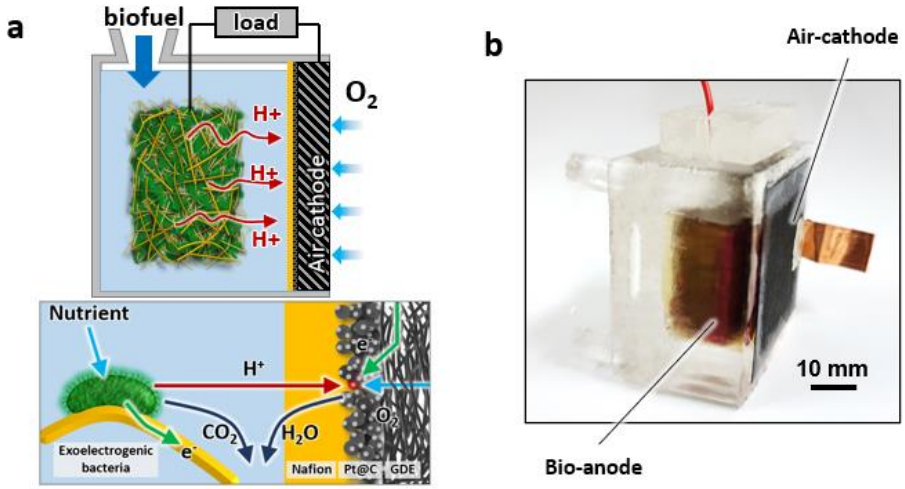

Figure 36. (a) The schematic illustration of the operating mechanism of a single-chamber MFC using AACNF as an anode electrode. **(b)** Photographic image of the customized MFC.

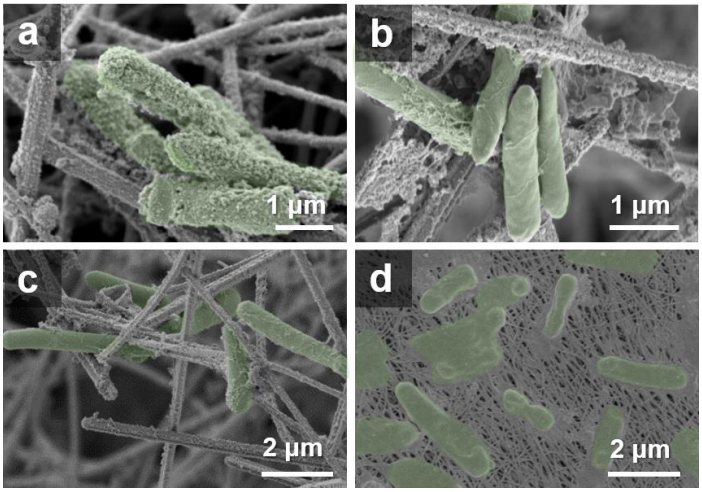

Figure 37. SEM images of the *geobacter anodireducens* culture inside the AACNF **(a-c)** and on the dense 2D network of NWs**(d)**.

SEM images demonstrated the volumetric interface between AACNF and *Geobacter Anodireducens*, compared to the 2D plannar network of NWs (**Figure 37**). The carbon paper-Pt@C-Nafion composite was employed as the air cathode, transforming hydrogen ions into water with oxygen. To evaluate the performance of the MFC, conventional fuel cell evaluation methods were adopted. The polarization curve shows the voltage generating ability of the fuel cell in current density loading variation. Similarly, the power density curve displays the performance of the fuel cell in a given current density. MFC requires settling time for microbes to cultivate and form the bio-hybrid electrode [55]. The polarization curve and power density curve indicate increased output as time passes on (**Figure 38a-b**).

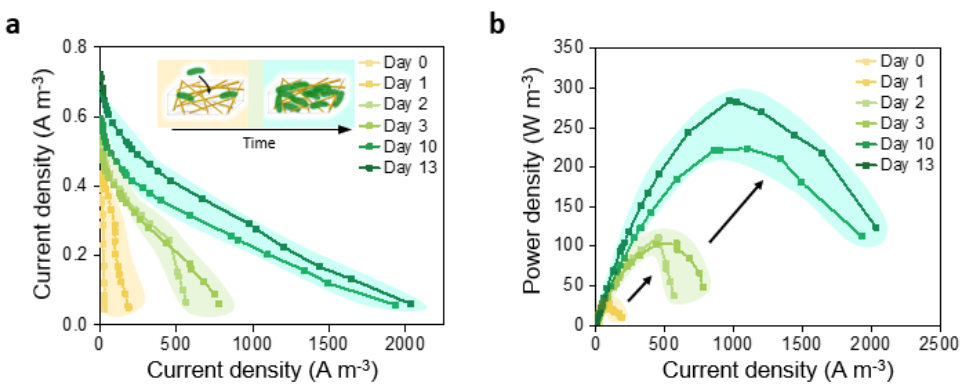

Figure 38. Polarization curve (a) and power density curve (b) of the MFC using AACNF as an anode with respect to the microbial culture time.

At Day 0-1, the MFC with AACNF(0.25 wt% of NWs) having dimensions of 20 mm x 20 mm and a thickness of 2 mm showed relatively low performance, which means low integration of Geobacters to AACNF. After a few days (Day 2-3), the MFC showed higher performance at over 100 W m^{-3}, indicating exponential growth

and denser incorporation to AACNF. Lastly, at a full integration state (Day 10-13), MFC showed power density as high as 283.09 W m^{-3}, which is considered to be high power density for MFCs with milliliter-scale volume. For in-depth analysis, we conducted an examination of the major loss factors in fuel cells, activation loss, ohmic loss, and concentration loss (**Figure 39**) .

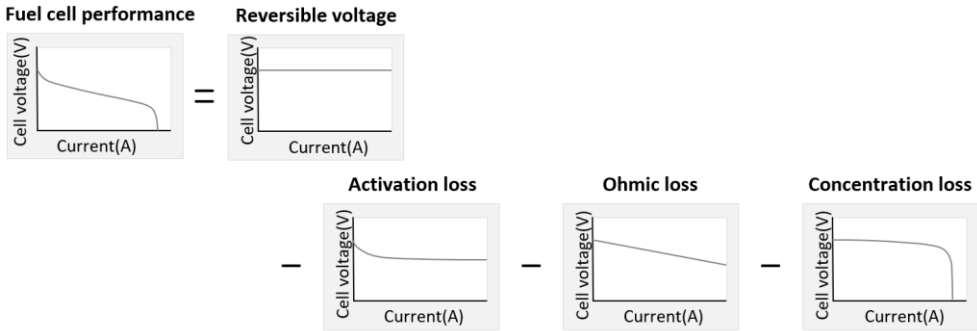

Figure 39. The analytic method of analyzing the polarization curve of a microbial fuel cell (MFC).

The polarization curve of fuel cells, which starts with the reversible voltage, is affected by four typical types of losses as shown above At low current densities, an initial rapid drop occurs, which is commonly known as activation loss caused by the activation kinetics of the electron transfer. In the moderate current density region, a linear voltage drop is observed throughout the entire section, which is called ohmic loss. In the high current density region, the voltage rapidly drops due to concentration loss.

As the microbes more cultivated, all three losses were reduced resulting in the significant imporved performance. When the microbes was less cultured (Day 0-3), the voltage drop occurs larger as the current increases, which leads to high ohmic resistance and low limit current density.

Next, we conducted the optimization process of the AACNF anode for the higher power density of the MFC system. To facilitate the interaction between microbes and the anode surface, we analyzed the performance trends according to the density of AACNF. **Figure 40a** describes the MFC performance trends by differentiating

the density of AACNF. We conducted parametric research on six different wt% of NWs, with five repetitive experiments each. Each AACNF was designed to have dimensions of 20 mm x 20 mm and a thickness of 2 mm. The polarization curve shows that there are optimal parameters (0.25 wt%, 0.5 wt%, and 1.0 wt% of NWs) with higher current density compared to dense conditions (2.0 wt% and 4.0 wt% of NWs) or sparse condition (0.15 wt% of NWs). In the case of AACNF with low-density NWs of 0.15 wt%, a limited number of microorganisms are able to form an effective bio-hybrid interface with the electrode, and the average distance between the microorganisms and the AACNF surface is increased. As a result, the electron transfer from microorganisms to AACNF becomes slower, leading to a larger activation loss (**Figure 40b-(i)**) [57, 58]. Conversely, for dense AACNFs (2.0 wt% and 4.0 wt% of NWs), the MFC exhibits a significantly high ohmic loss and low limit current density (**Figure 40b-(ii-iii)**). This phenomenon can be attributed to two factors: the surface area of active sites where the interaction between microorganisms and AACNF occurs, and the mass transfer ratio of the nutrients. Given the size of Geobacter anodireducens, which ranges from 1 μm to 5 μm, the microorganisms cannot uniformly penetrate inside the thickly composed AACNF, leaving a non-effective area of the inner surface of AACNF. Thus, the lack of active sites where microorganisms and AACNF interact leads to a decrease in efficiency as the current density increases. Furthermore, the low mass diffusivity of nutrients due to decreased porosity is an additional reason for the low limit current density and maximum power density (**Figure 40b-(iii-iv)**). In the case of sparsely constructed AACNF (0.15 wt% of NWs), microorganisms penetrate well inside the AACNF, yet exhibit low limit current density and maximum power density. It is suggested that the decrease in the active site area is caused by the low quantity of

NWs. Taking all these factors into account, it is determined that the AACNF with intermediate density (0.25 wt%, 0.5 wt%, and 1.0 wt% of NWs) is suitable for efficient MFC operation. The MFC using AACNF with 0.5 wt% of NWs achieved a maximum power density of up to 330 W m^{-3}.

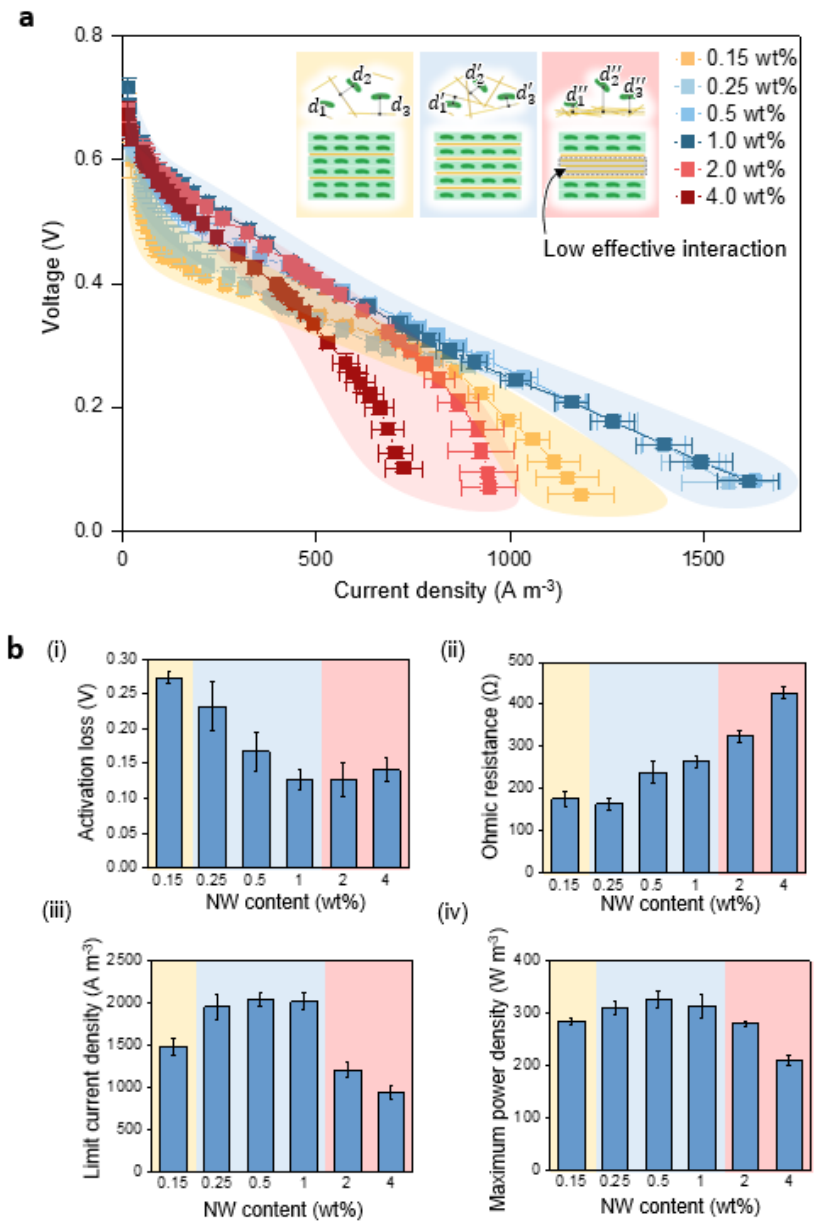

Figure 40. (a) Polarization curves of the MFC with varying densities of the AACNF. The error bars are the standard deviation (s.d.) for $N = 5$ samples**. (b)**

Activation loss (i), ohmic resistance (ii), limit current density (iii), and maximum power density (iv) of the MFC with varying densities of the AACNF. The error bars are the s.d. for N = 5 samples.

Finally, Long term stability of the MFC using AACNF as an anode was examined by the 25 days of operation (**Figure 41**). The alterations observed in the maximum power density of MFC due to nutrient depletion and subsequent resupply demonstrate a general tendency of MFC systems.

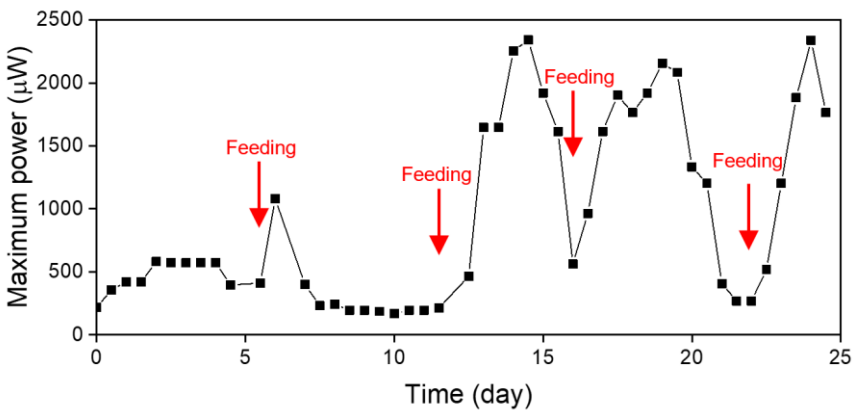

Figure 41. MFC maximum power against time for 25 days of long-term operation. The red arrow indicates the basal broth supply to the *Geobacter anodireducens* culture. The AACNF anode had dimensions of 20 mm x 40 mm and a height of 20 mm with 0.25 wt% of NW density.

4.3. Method

Preparation of the PAAm hydrogel-embedded AACNF

PAAm hydrogel precursor solution was prepared by dissolving AAm as a monomer, MBA as a crosslinker, and APS as an initiator. The weight percent of AAm is 18%, and the weight ratio between AAm, MBA, and APS was 1:0.0007:0.0045. Then, we gently replaced the solution contained in the existing AACNF with a PAAm hydrogel precursor solution. Finally, the PAAm hydrogel solution within the AACNF was thermally polymerized at 60 ℃ for 3 h. Schematic illustration of the fabrication process is described in **Figure S7**.

Preparation of the PEDOT:PSS hydrogel-embedded AACNF

PEDOT:PSS aqueous dispersion was permeated into the AACNF and allowed to fully diffused at room temperature for 2 h. The AACNF with PEDOT:PSS solution is treated with 0.005 volume fraction of sulfuric acid at 90℃ for 3h.

Preparation of the *Geobacter anodireducens* culture

The biological resources used in this research were distributed from Korean Collection for Type Cultures (KCTC). The basal medium for the *Geobacter anodireducens* (=CGMCC 1.12536 = KCTC 4672) was prepared by referring to KCTC. It was prepared by containing 1.3124 g of sodium acetate, 4 g of $NaHCO_3$, 2.4 g of NH_4Cl, 0.96 g of NaH_2P_4, 0.16 g of KCl, 7.84 g of ferric citrate, and 6.4 g of nutrient broth (Difco™ Nutrient Broth; BD) in 1 L DI water.

Preparation of the Air cathode

The Microporous Layer (MPL) of the Carbon paper (Sigracet 22 BB; NARA CELL TECH CORP.) was spray-coated with 250 μL of Pt/C catalyst ink (30 mg /g Pt, 10 mg/g Nafion™ in 1 g Electro Catalyst Ink; Fuel Cell Earth) in 10 mL isopropyl alcohol (IPA) and 500 μL Nafion solution (Nafion™ D-521 dispersion, 5% w/w in water and 1-propanol; Thermo Fisher Scientific Inc.) in 10 mL IPA in order.

Electrical characterization of the PAAm hydrogel-embedded AACNF with external tensile strain.

Two 3D-printed anchor structures were placed at both ends of the Ecoflex mold. AACNF was synthesized between these anchors and cleaned multiple times with DI water. Then, gold-plated contact clips were used to grip the AACNF portion of both anchors to wire both ends of the AACNF. The solution inside the AACNF was then replaced with a PAAm hydrogel precursor solution, and the PAAm hydrogel solution within the AACNF was thermally polymerized at 60 ℃ for 3 h. The electrical resistance between both ends of the PAAm hydrogel-embedded AACNF with external strain was measured by the DMM (PXI-4065; National Instruments). Stretching was applied to the sample by the linear stage (VT-80; PI). The electrical conductivities of the samples were calculated by the following equation: $\sigma = L/(R \cdot A)$. Photographic images of the measurement process are described in **Figure 34**.

Geobacter anodireducens fixation for SEM imaging

AACNF with *Geobacter anodireducens* culture was fixed by 5% glutaraldehyde solution (25% in H_2O; Sigma Aldrich) for 1 h and was cleaned with distilled water. The cleaned sample was dehydrated by 20%, 40%, 60%, 80%, and 100% ethanol solution in order. Then, the additional fixation was applied to the samples with an aqueous 1% osmium tetroxide (OsO4; Heraeus Precious Metals GmbH & Co. KG) solution for 8 h. Finally, platinum with a less than 10 nm thickness was coated to the prepared samples before visualizing them through FE-SEM.

Measurement of polarization curve for microbial fuel cells

The polarization curve of the MFC was obtained using a custom-built digital potentiometer. The device was equipped with programmable rheostats (MAX5484; Maxim Integrated) to provide various loads. To control the peripherals and enable wireless communication, we employed a microcontroller unit (MCU: ESP32; Espressif Systems). The MCU was programmed to regulate the rheostats and receive the MFC voltage via an analog-digital-converter. The resistance value of the rheostats was swept from high to low until $dV/dt < 1$ mV s^{-1}. In addition, to facilitate wireless data transmission, we developed an MCU-run Web-server that sends and plots data to smartphones through Wi-Fi communications.

5. Conclusion and Perspectives

In summary, we have successfully synthesized a 3D porous electrode based on Ag-Au core-shell nanowires through a simple one-step solution process. The nano-welding at the AgNWs junctions by Au coating has resulted in a robust 3D percolation network with high chemical stability from its Au shells and high electrical conductivity from its core AgNWs. By optimizing the three fabrication parameters —Ethanol concentration, Au against Ag ratio, and the precursor concentration—, we have achieved the mold-fitted AACNF with over 99.9% porosity, ultralow density, and high electrical conductivity.

The mass transportation feature through the porous AACNF was investigated for both nano-meter-sized and micro-meter-sized substances. Nano-meter-size substances, such as AAm and PEDOT:PSS polymer, diffused well inside the AACNF and could further form a hierarchical hydrogel network within the AACNF. The hierarchical structure of AACNF with PAAm hydrogel network exhibited high electrical conductivity due to AACNF's pre-formed nano-welding. For micrometer-size substances, living cells were successfully embedded within the AACNF of low density and indicating the biocompatibility of AACNF. Furthermore, the MFC using AACNF as an anode showed high power density performance. An effective 3D interface between electrode surface and microbes was investigated regarding the unique structure of AACNF.

We anticipate that AACNF holds great potential for various areas due to its unique properties and advantages. The ultra-porous structure enables effective electrochemical reactions and mass transport, making it highly suitable for various energy devices like batteries, supercapacitors, and fuel cells. Further enhancement

of electrochemical properties could be achieved through additional coating process or incorporation of functional microparticles or conductive hydrogels. Moreover, the high level of bio-hybrid integration of AACNF makes it a promising candidate for novel bio-hybrid electrodes with enhanced biochemical activity detection or energy harvesting capabilities.

Bibliography

[1] A. Vu, Y. Qian, A. Stein, Advanced Energy Materials 2012, 2, 1056.

[2] Z. Chen, D. L. Danilov, R. A. Eichel, P. H. Notten, Advanced Energy Materials 2022, 12, 2201506.

[3] R. Kitaura, N. Imazu, K. Kobayashi, H. Shinohara, Nano letters 2008, 8, 693.

[4] L. Shi, W. Yang, X. Zha, Q. Zeng, D. Tu, Y. Li, Y. Yang, J. Xu, F. Chen, Colloids and Surfaces A: Physicochemical and Engineering Aspects 2022, 652, 129862.

[5] F. Bu, M. M. Zagho, Y. Ibrahim, B. Ma, A. Elzatahry, D. Zhao, Nano Today 2020, 30, 100803.

[6] C. Ma, Q. Fan, M. Dirican, Y. Song, X. Zhang, J. Shi, Journal of Materials Science 2020, 55, 16323.

[7] S. Yang, Y. Li, Q. Chen, Journal of Materials Chemistry A 2021, 9, 14025.

[8] U. Krewer, T. Turek, Electrochemical Science Advances 2023, 3, e2300001.

[9] J. Zou, J. Liu, A. S. Karakoti, A. Kumar, D. Joung, Q. Li, S. I. Khondaker, S. Seal, L. Zhai, ACS Nano 2010, 4, 7293.

[10] W. Zhao, Y. Li, S. Wu, D. Wang, X. Zhao, F. Xu, M. Zou, H. Zhang, X. He, A. Cao, ACS Applied Materials & Interfaces 2016, 8, 34027.

[11] M.-H. Lee, Y. H. Kang, J. Kim, Y. K. Lee, S. Y. Cho, Advanced Energy Materials 2019, 9, 1900914.

[12] Z. Chen, C. Xu, C. Ma, W. Ren, H.-M. Cheng, Advanced Materials 2013, 25, 1296.

[13] X.-H. Li, X. Li, K.-N. Liao, P. Min, T. Liu, A. Dasari, Z.-Z. Yu, ACS Applied Materials & Interfaces 2016, 8, 33230.

[14] S. Gupta, S. K. Sharma, D. Pradhan, N.-H. Tai, Composites Part A: Applied Science and Manufacturing 2019, 123, 232.

[15] Z. Wu, C. Xu, C. Ma, Z. Liu, H.-M. Cheng, W. Ren, Advanced Materials 2019, 31, 1900199.

[16] C. Androulidakis, M. Kotsidi, G. Gorgolis, C. Pavlou, L. Sygellou, G. Paterakis, N. Koutroumanis, C. Galiotis, Scientific Reports 2021, 11, 13548.

[17] S. Shi, B. Qian, X. Wu, H. Sun, H. Wang, H.-B. Zhang, Z.-Z. Yu, T. P. Russell, Angewandte Chemie International Edition 2019, 58, 18171.

[18] Z. Lin, J. Liu, W. Peng, Y. Zhu, Y. Zhao, K. Jiang, M. Peng, Y. Tan, ACS Nano 2020, 14, 2109.

[19] Y. Tang, S. Gong, Y. Chen, L. W. Yap, W. Cheng, ACS nano 2014, 8, 5707.

[20] S. M. Jung, D. J. Preston, H. Y. Jung, Z. Deng, E. N. Wang, J. Kong, Advanced Materials 2016, 28, 1413.

[21] F. Qian, P. C. Lan, M. C. Freyman, W. Chen, T. Kou, T. Y. Olson, C. Zhu, M. A. Worsley, E. B. Duoss, C. M. Spadaccini, T. Baumann, T. Y.-J. Han, Nano Letters 2017, 17, 7171.

[22] Y.-J. Wan, P.-L. Zhu, S.-H. Yu, R. Sun, C.-P. Wong, W.-H. Liao, Small 2018, 14, 1800534.

[23] Y. Chen, L. Zhang, C. Mei, Y. Li, G. Duan, S. Agarwal, A. Greiner, C. Ma, S. Jiang, ACS Applied Materials & Interfaces 2020, 12, 35513.

[24] F. Peng, W. Zhu, Y. Fang, B. Fu, H. Chen, H. Ji, X. Ma, C. Hang, M. Li, ACS Applied Materials & Interfaces 2023, 15, 4284.

[25] X. Li, S. Yang, J. Sun, P. He, X. Xu, G. Ding, Carbon 2014, 78, 38.

[26] S. Wu, M. Zou, Z. Li, D. Chen, H. Zhang, Y. Yuan, Y. Pei, A. Cao, Small 2018, 14, 1800634.

[27] S. Zhao, H.-B. Zhang, J.-Q. Luo, Q.-W. Wang, B. Xu, S. Hong, Z.-Z. Yu, ACS Nano 2018, 12, 11193.

[28] Z. Wang, Y. Wang, Y. Chen, M. Yousaf, H. Wu, A. Cao, R. P. S. Han, Advanced Functional Materials 2019, 29, 1807467.
[29] C. Weng, G. Wang, Z. Dai, Y. Pei, L. Liu, Z. Zhang, Nanoscale 2019, 11, 22804.
[30] J. D. Afroze, L. Tong, M. J. Abden, Z. Yuan, Y. Chen, Carbon 2021, 175, 312.
[31] Z. Deng, P. Tang, X. Wu, H.-B. Zhang, Z.-Z. Yu, ACS Applied Materials & Interfaces 2021, 13, 20539.
[32] T. M. Day, P. R. Unwin, N. R. Wilson, J. V. Macpherson, Journal of the American Chemical Society 2005, 127, 10639.
[33] S. Wang, X. Zhao, T. Cochell, A. Manthiram, The journal of physical chemistry letters 2012, 3, 2164.
[34] X. Xia, J. Tu, Y. Zhang, X. Wang, C. Gu, X.-b. Zhao, H. J. Fan, ACS nano 2012, 6, 5531.
[35] N. Choudhary, C. Li, H.-S. Chung, J. Moore, J. Thomas, Y. Jung, ACS nano 2016, 10, 10726.
[36] H. Lee, S. Hong, J. Lee, Y. D. Suh, J. Kwon, H. Moon, H. Kim, J. Yeo, S. H. Ko, ACS Applied Materials & Interfaces 2016, 8, 15449.
[37] S. Huang, Y. Liu, M. Jafari, M. Siaj, H. Wang, S. Xiao, D. Ma, Advanced Functional Materials 2021, 31, 2010022.
[38] W. Jeong, S. Lee, H. Choi, J. Bae, S.-H. Lee, Y. Ma, S. Yoo, J.-H. Ha, J.-I. Hong, S. Park, K. Woo, J.-H. Choi, S. Lee, Materials Today 2022, 61, 30.
[39] Y. Zhu, S. Kim, X. Ma, P. Byrley, N. Yu, Q. Liu, X. Sun, D. Xu, S. Peng, M. C. Hartel, Nano Research 2021, 14, 4294.
[40] K. K. Kim, M. Kim, K. Pyun, J. Kim, J. Min, S. Koh, S. E. Root, J. Kim, B.-N. T. Nguyen, Y. Nishio, S. Han, J. Choi, C. Y. Kim, J. B. H. Tok, S. Jo, S. H. Ko, Z. Bao, Nature Electronics 2023, 6, 64.
[41] S. Choi, S. I. Han, D. Jung, H. J. Hwang, C. Lim, S. Bae, O. K. Park, C. M. Tschabrunn, M. Lee, S. Y. Bae, Nature nanotechnology 2018, 13, 1048.
[42] S.-H. Sunwoo, S. I. Han, H. Kang, Y. S. Cho, D. Jung, C. Lim, C. Lim, M.-j. Cha, S.-P. Lee, T. Hyeon, D.-H. Kim, Advanced Materials Technologies 2020, 5, 1900768.
[43] T.-H. Yang, J. Ahn, S. Shi, D. Qin, ACS Nano 2021, 15, 14242.
[44] M. Guettari, A. Belaidi, S. Abel, T. Tajouri, Journal of Solution Chemistry 2017, 46, 1404.
[45] M. M. Tomadakis, T. J. Robertson, Journal of Composite Materials 2005, 39, 163.
[46] H. Liu, X. Liu, Z. Liu, J. Tao, X. Dai, Q. Yang, J. Xu, Z. Shan, Inorganic Chemistry Frontiers 2021, 8, 4395.
[47] Y. Hu, B. Yu, X. Qi, B. Shi, S. Fang, Z. Yu, J. Yang, Journal of Materials Science 2020, 55, 10155.
[48] Y. Hou, N. Jiang, D. Sun, Y. Wang, X. Chen, S. Zhu, L. Zhang, RSC advances 2020, 10, 4907.
[49] B. N. Narasimhan, G. S. Deijs, S. Manuguri, M. S. H. Ting, M. Williams, J. Malmström, Nanoscale Advances 2021, 3, 2934.
[50] R. da Silva Fernandes, F. C. Tanaka, C. R. F. Junior, U. G. Yonezawa, M. R. de Moura, F. A. Aouada, Journal of Polymer Research 2022, 29, 519.
[51] B. Yao, H. Wang, Q. Zhou, M. Wu, M. Zhang, C. Li, G. Shi, Advanced Materials 2017, 29, 1700974.
[52] A. D. Castiaux, D. M. Spence, R. S. Martin, Analytical Methods 2019, 11, 4220.
[53] N. Chaicharoenaudomrung, P. Kunhorm, P. Noisa, World journal of stem cells 2019, 11, 1065.
[54] S. Thippabhotla, C. Zhong, M. He, Scientific reports 2019, 9, 13012.
[55] R. P. Ramasamy, Z. Ren, M. M. Mench, J. M. Regan, Biotechnology and bioengineering 2008, 101, 101.
[56] B. E. Logan, B. Hamelers, R. Rozendal, U. Schröder, J. Keller, S. Freguia, P. Aelterman, W. Verstraete, K. Rabaey, Environmental science & technology 2006, 40, 5181.
[57] X. Xie, L. Hu, M. Pasta, G. F. Wells, D. Kong, C. S. Criddle, Y. Cui, Nano letters

2011, 11, 291.
[58] N. Sekar, R. P. Ramasamy, J Microb Biochem Technol S 2013, 6, 1.
[59] L. J. Andrés, M. F. Menéndez, D. Gómez, A. L. Martínez, N. Bristow, J. P. Kettle, A. Menéndez, B. Ruiz, Nanotechnology 2015, 26, 265201.

[60] A. El-kharouf, T. J. Mason, D. J. L. Brett, B. G. Pollet, J. power sources, 2012, 218, 393-404.

[61] M. Sansotera, W. Navarrini, M. Gola, C. L. Bianchi, P. Wormald, A. Famulari, M. Avataneo, Journal of Fluorine Chemistry, 2011, 132, 12, 1254-1261

[62] F. Conrado, M. Pavese. *Journal of Nanomaterials*, 2017, 11.

[63] Chen, J., Zheng, H., Kang, J., Yang, F., Cao, Y., & Xiang, M. *RSC advances*, 2017, *7*(5), 3035-3042.

[64] Langley, D., Giusti, G., Mayousse, C., Celle, C., Bellet, D., & Simonato, J. P., *Nanotechnology*, 2013, *24*(45), 452001.

[65] Zhang, F. Y., Advani, S. G., & Prasad, A. K., *Journal of power sources*, 2008, *176*(1), 293-298.

국문 초록

은-금 코어-쉘 나노와이어의 3차원적 조립을 통한 고다공성·고전도성·생체친화성 템플릿 전극

최준화
기계공학부
서울대학교 대학원

템플릿 전극은 에너지 소자, 생체전극 등 기능성 전극의 기본골격으로서 활용되어 최종적인 응용에서 전체적인 성능에 결정적인 영향력을 가질 수 있는 중요한 요소이다. 코어-쉘 나노와이어는 코어 및 쉘 물질의 상호보완적 효과로 인해 차세대 템플릿 전극의 기본 재료로서 높은 기대를 받고 있으나, 최종적인 전극의 형상적 한계나 제조 공정상의 확장성 제약 등의 문제로 인해 실용적인 응용에는 제한이 있는 상황이다. 본 연구에서는 나노 웰딩 합성 기법을 기반으로, 원스텝 공정을 사용하여 제작할 수 있는 고다공성 Ag-Au 코어-쉘 나노와이어 폼(AACNF)을 소개한다. AACNF는 금속 기반 전극 중에서도 가장 낮은 밀도를 가지면서도, 이례적으로 높은 전기전도도(99.33-753.04 S m^{-1})를 보여주었으며, 우수한 물질 전달 특성으로 인해 고분자 전구체와 생체세포와 같은 다양한 기능성 물질과 다중 규모의 계층 구조를 형성할 수 있음을 확인하였다. AACNF의 합성과정에서 동반되는 나노 웰딩 현상으로 인해 AACNF는 기계적 인장에 대해 높은 안정성을 가졌으며, 하이드로겔 등의 이차물질과 계층적인 방식으로 융합하였을 때 단순히 혼합한 형태와 비교하여 10,000배 이상 높은 전도도를 나타내었다. AACNF는 공극의 크기도 마이크로미터 수준이 되도록 조절이 가능하며, 섬유아세포와 외전기성 미생물 등 1-10 μm 규모의 큰 입자들도 내부로 침투하여 계층적인 융합이 가능하였다, 특히, AACNF 기반 미생물 연료전지는 최적

의 밀도 범위 내에서 높은 출력밀도(~ 330.1 W m^{-3})를 기록하여 생체 전극 및 에너지 소자용 전극으로서의 가능성을 확인하였다. AACNF는 그 고유한 특성으로 인해 다양한 크기 규모의 물질들과 계층 구조를 형성하는 데 있어서 향후 진보된 에너지 장치 및 생체융합 전극 분야 템플릿 전극으로서 폭넓게 활용될 수 있을 것으로 기대된다.

주요어 : 은-금 코어-쉘 나노와이어, 3차원 퍼콜레이션 네트워크, 다공성 템플릿 전극, 바이오하이브리드 전극
학 번 : 2018-25366